学位申請論文

小沢 恭一郎

STUDY OF ρ/ω MESON MASS MODIFICATION IN NUCLEAR MATTER

Kyoichiro Ozawa

A dissertation submitted in partial fulfillment of
the requirements for the degree of

Doctor of Science

Department of Physics
Kyoto University

Abstract

We have measured invariant mass spectra of electron-positron pairs in the target rapidity region of 12GeV p+A reactions with a newly constructed spectrometer at the primary beam line in KEK Proton Synchrotron. The aim of the experiment was to detect in-medium modification of the vector meson mass, which is theoretically predicted as a consequence of partially-restored chiral-symmetry at normal nuclear-matter density. The observed invariant mass spectra of electron-positron pairs show a clear peak of $\omega \rightarrow e^+e^-$ decays. It is a first observation in p+A reaction in this energy region. We have observed a significant difference in the mass spectra between p+C and p+Cu interactions as an excess of yield at the low mass side of the ω meson The number of the excess of the light target is 19.6 ± 11.7 and that of the copper target is 29.5 ± 8.7. The excess is statistically significant for the copper target data. The ratios to the amplitude of the ωpeak are 0.26 ± 0.16 for the light target and 1.48 ± 0.56 for the copper target. The difference between the two cases should be originated from the difference of the nuclear size. The natural explanation of the shape change is that the mass modification of ρ/ω mesons takes place inside a nucleus. This is the first observation of the leptonic in-medium decay of the vector mesons at normal nuclear-matter density.

Contents

Chapter 1

Introduction

In the summer of 2000 at the Relativistic Heavy Ion Collider (RHIC) in the Brookhaven National Laboratory (BNL), the first gold-gold collisions were observed [1] and a new era of hadron physics has started. In February 2000 before the start of the RHIC experiments, CERN (European Organization for Nuclear Research) summarized their history of the experiments on the heavy ion program investigating physics of hot and/or dense nuclear matter at the Super Proton Synchrotron (SPS) [2]. They combined the results of 7 experiments, NA44, CERES/NA45, NA49, NA50, NA52, WA97/NA57 and WA98 [3, 4, 5, 6, 7, 8, 9], and concluded the observation of tantalizing hints for the existence of a new state of matter in which quarks, instead of being bound into a complex particle, such as proton and neutron, are liberated to move freely.

The supportive evidences for this new state of matter are based on a multitude of different observations and one of these is the measurement of correlated electron-positron pairs. The CERES/NA45 collaboration measured low-mass electron-pair productions in Pb-Au collisions at 158 A GeV [4]. The observed spectra of e^+e^- pairs is shown in Figure 1.1. They observed an enhancement of e^+e^- pair yield in the mass range $0.3 < m_{ee} < 0.7 \, \text{GeV/c}^2$ over the expected yield from the known hadronic sources in pBe collisions. This observation is very important since the effect could be understood as a consequence of the mass modification of the ρ and ω meson in hot matter, and such a modification is theoretically predicted as partial or complete restoration of the chiral symmetry in hot and/or dense nuclear matter [10, 11]. Although many heavy-ion experiments were carried out in CERN-SPS and also at Alternating Gradient Synchrotron (AGS) in BNL to study hot and

dense matter, CERES was only an experiment which could address experimental information on the mass modification of vector mesons. Because among these experiments only CERES spectrometer had the capability of identifying electron. However they archived the invariant mass resolution of several tens MeV/c^2, the experiment which had higher resolution is needed.
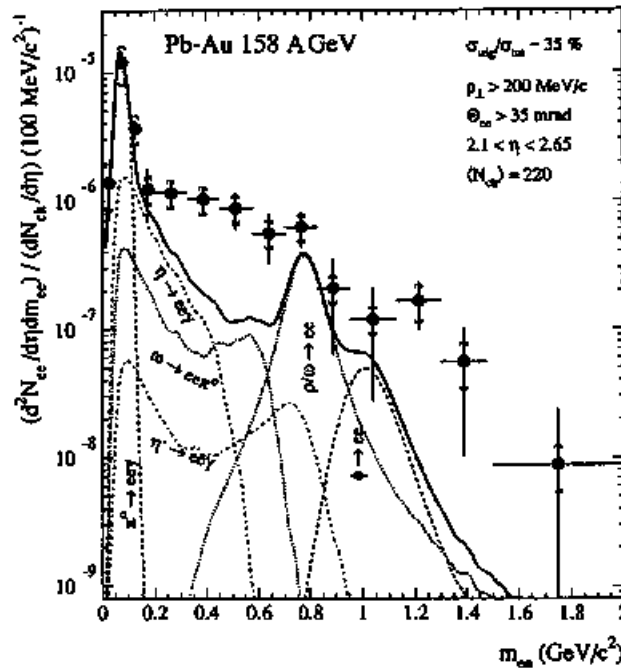
Figure 1.1: Inclusive invariant e^+e^- mass spectrum in 158 A GeV Pb-Au collisions normalized to the observed charged-particle density [4]. The statistical errors of the data are shown as bars, the systematic errors are given independently as brackets. The full line represents the e^+e^- yield from the hadron decays scaled from proton-induced collisions. The contributions of individual decay channel are also shown.

The theoretical aspect of the meson modification in nuclear matter is generally described as follows, in QCD the mass of the vector mesons is mainly determined by the effective mass of quark, known as constituent quark mass. The effective mass is induced by the dynamical breaking of chiral symmetry

in QCD. In hot and/or dense matter this broken symmetry is subject to restore partially or completely, and hence the mass of vector mesons can be modified [12, 13, 14].

There are, however, very few experimental inputs available and acquisition of more experimental information is important to understand the role of the chiral symmetry breaking in hadronic states. In high-energy heavy-ion experiment, such as CERES, the time evolution of temperature and density is inevitable, which makes the theoretical interpretation of the data extremely difficult. On the other hand, the measurements of such mesons, which are produced and decays in a nucleus, are of great interest, since the density in a nucleus is rather constant. Another attractive point of the measurements in constant density is that a significant decrease of $\bar{q}q condensates, \langle \bar{q}q \rangle$, is expected not only at high temperature but also at the normal nuclear density. Here, the $\bar{q}q$ condensates $\langle \bar{q}q \rangle$ is an order parameter of the chiral symmetry of the QCD vacuum and its dependence on temperature and density of the matter is theoretically predicted as shown in Figure 1.2 [15].
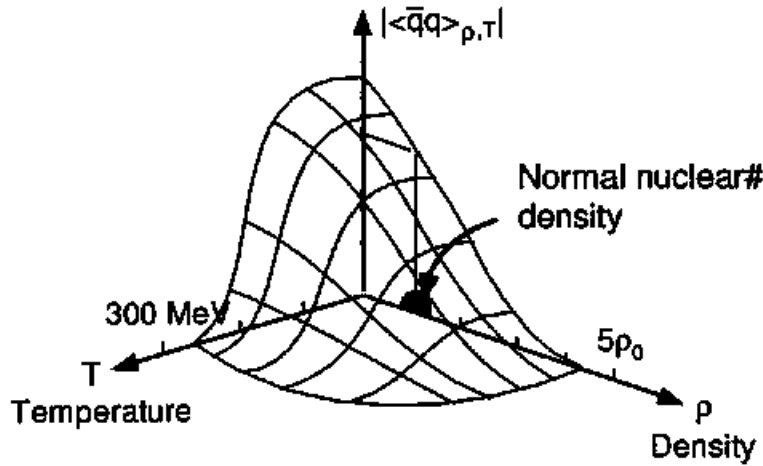
Figure 1.2: The dependence of the $\bar{q}q$ condensates $\langle \bar{q}q \rangle$ on temperature and density of the matter

Using the QCD sum rule, Hatsuda and Lee predicted in-medium modification of the vector mesons [13]. Their prediction on the density dependence of meson masses is shown in Figure 1.3. According to this model, mass decrease at normal nuclear density is $120 \sim 180$ MeV/c^2 for the ω and ρ mesons

and $20 \sim 40$ MeV/c^2 for the ϕ meson.

To investigate the in-medium properties of the vector mesons at normal nuclear-matter density, several experimental efforts including the present experiment are in place [16, 17, 18, 19, 20, 21]. An experiment had been done by TAGX collaboration at INS [16]. They reported the observation of modified ρ meson in $\pi^+\pi^-$ invariant mass spectra in ^{3}He$(\gamma, \pi^+\pi^-)$X channel [16]. However the π meson channel is not free from the effect of final state interactions, further experimental data, especially in the lepton-pair channel, are awaited. Another experiment had been done by the Dilepton Spectrometer (DLS) at LBNL [17]. They observed an excess in the mass region below 0.7 GeV/c^2 over the expected sources. Since the DLS data and also the TAGX data were based on the sub-threshold ρ-meson production and not free from the influence of the limited phase space, higher energy experiment is needed. There is an experiment HADES at GSI in preparation, which measures invariant mass spectra of e^+e^- pairs up to 1 GeV/c^2, using 1.0 A GeV/c^2 heavy ion beam or hadron beams up to a few GeV/c^2 [18].

The present experiment, KEK-PS E325, was designed to measure the decays of the vector mesons, $\phi \to e^+e^-$, $\rho/\omega \to e^+e^-$ and $\phi \to K^+K^-$, with better mass resolution than before in the kinematical region where the decay probability inside a target nucleus was enhanced ($0.6 < y_{ee} < 2.2$, $0.0 < P_{Tee} < 1.5$ GeV/c, where y_{ee} is rapidity and P_{Tee} is transverse momentum of electron-positron pairs). Expected deformation of the invariant mass spectra of $\rho/\omega \to e^+e^-$ with $\beta\gamma_{lab}$ of about 1.0 are shown in Figure 1.4. To calculate the spectra, we take following assumptions; 1) mass shift as predicted by Hatsuda and Lee (Figure 1.3), 2) in-media broadening of decay width is three time larger than in free space as suggested by D. Cabera *et al.* [22], 3) production of ρ/ω occurs at the surface of a nucleus which is expected from the A$^{2/3}$ dependence of the production cross section [23]. In Figure 1.4 we can see the excess corresponding to the ρ/ω's decaying inside a nucleus on the left side of the main peak due to the ω's decaying outside the nucleus. These signatures are unique to obtain the experimental information for the mass modification of ρ/ω mesons in nuclear matter, because 1) we can expect significant mass-shape modification, and 2) the shape difference should be nuclear-size dependent.

In this paper we report the study of the e^+e^- invariant spectra measured in the 12-GeV p+A reaction. The spectrometer was built at the primary beam line EP1-B in the 12GeV-PS at KEK. We have been taking the data since 1998, and this manuscript describes the e$^+$e$^-$ triggered data of 5.6 $\times$
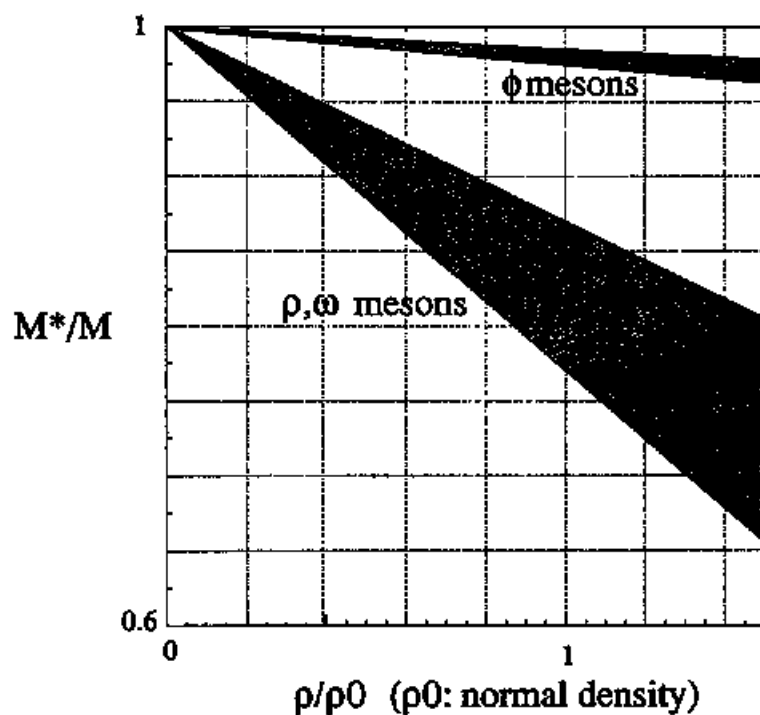
Figure 1.3: Expected mass shift of the vector mesons (ρ, ω and ϕ) as a function of baryon density normalized at $\rho = \rho_0$. The ambiguity of the theoretical predictions are shown as a band which is caused in estimating the quark condensates from limited experimental information. The error for ρ and ω mesons is from $\langle \overline{u}u + \overline{d}d \rangle_N$, the u and d quark condensation in a nucleon [13].
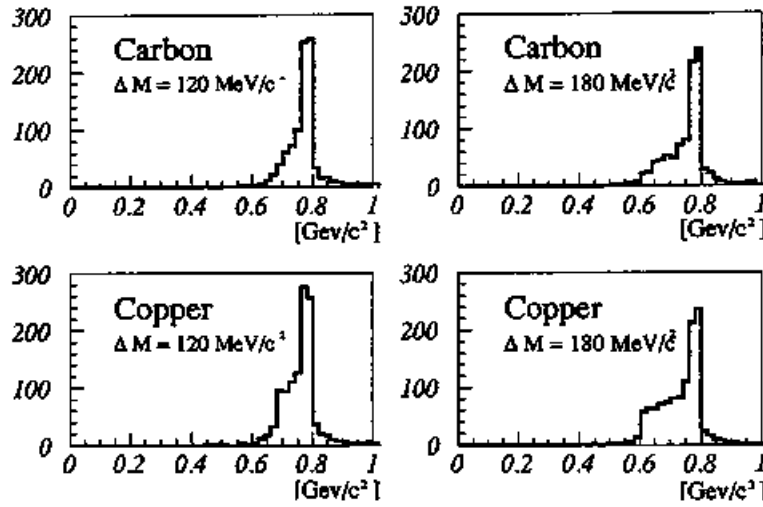
Figure 1.4: Expected invariant mass spectra of $\rho/\omega \to e^+e^-$: As the mass shift of ρ and ω meson, we used 120 MeV/c^2 and 180 MeV/c^2 which correspond to the upper and the lower curves in Figure 1.3, respectively. The difference in the mass shapes is visible between the carbon and the copper targets. We assumed that the decay widths of ρ and ω are three times larger in the nuclear medium than in the free space [22].

10^7 events collected in 1998 using 2.1×10^{14} protons on the targets.

In Chapter 2, the experimental procedure is described. The detail of the analysis procedure is presented in Chapter 3. In Chapter 4 we present the data of the e^+e^- invariant mass spectra, and discussion are made on the nuclear mass dependence of the observed e^+e^- spectra. The conclusion is given in Chapter 5.

Chapter 2

Experimental procedure

2.1 Over view of the apparatus

A double-arm spectrometer was built at the primary beam line EP1-B in the 12GeV Proton Synchrotron (PS) at the High Energy Accelerator Research Organization (KEK). The beam line EP1-B was newly constructed for experiments requiring a primary beam [24]. This beam line was designed to transport 12 GeV protons with the maximum intensity of 4×10^9 per 2 seconds spill, without a beam halo.

We measured the invariant mass spectra both in the e^+e^- channel for the $\rho/\omega/\phi$ meson decays and in the K^+K^- channel for the ϕ meson decays with the same apparatus.

There are two key points in this experiment. First is to detect slowly moving vector mesons which have a larger probability to decay inside nucleus. The typical acceptance for the ω mesons was $0.6 < y_{ee} < 2.2$ and $1 < \beta\gamma_{ee} < 4$. Second is to use high quality primary beam on thin targets. The combination of the intense beam with the thin targets were essential to keep the gamma conversion rate below the Dalitz decay rate. The typical interaction rate was as high as 1.2 MHz.

The layout of the detectors is shown in Figure 2.1 and 2.2[1] The spectrometer had two electron arms and two kaon arms, which shared a dipole magnet and tracking devices. The electron arms covered from ±12 degrees to

---

[1]In this manuscript, we adopt the right-handed coordinate system of which the origin is at the center of the spectrometer magnet, the x-axis is the normal beam direction, and the z-axis is vertical pointing upward
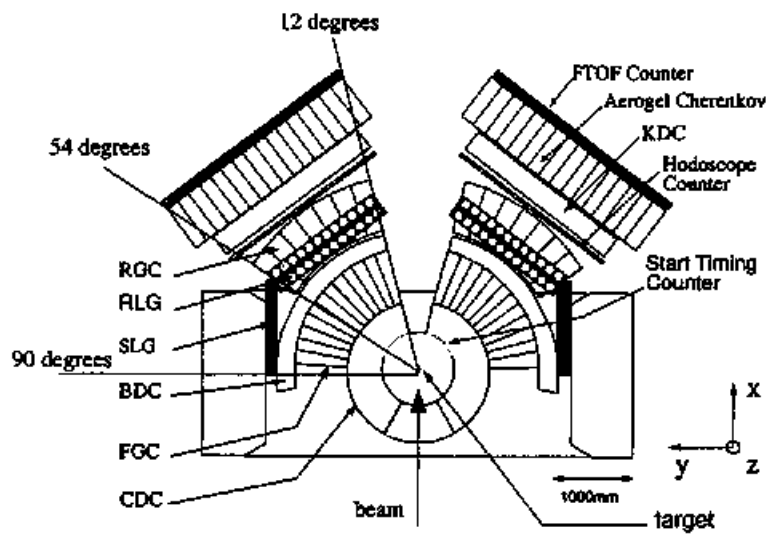
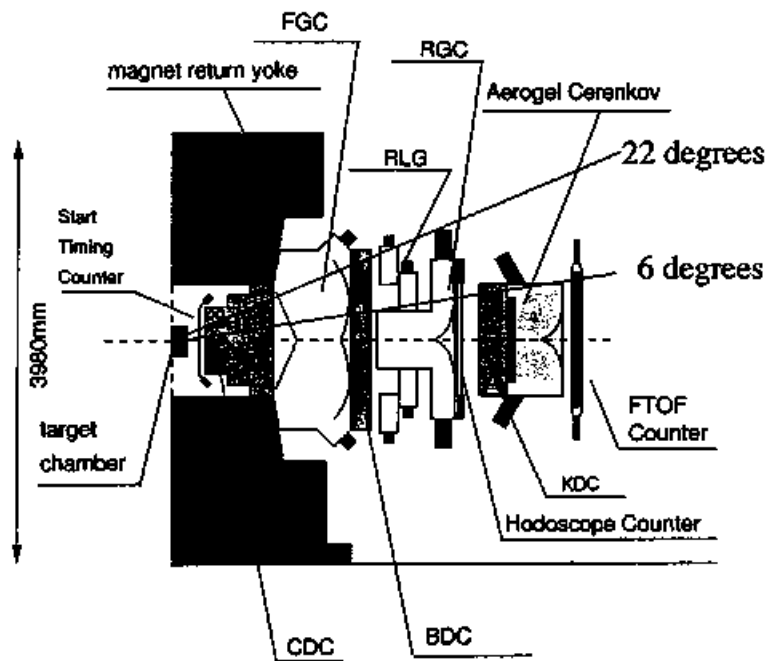Figure 2.1: Schematic view of the E325 spectrometer, the top view.

Figure 2.2: Schematic view of the E325 spectrometer, the cross section along the center of the kaon arm is shown.

±90 degrees horizontally and ±22 degrees vertically. The kaon arms covered from ±12 degrees to ±54 degrees horizontally and ±6 degrees vertically.

During the experimental period described in this manuscript, primary protons with a typical intensity of 7×10^8 Hz were delivered to the targets at the center of the dipole magnet. We used three kinds of targets aligned in-line, carbon, copper, and polyethylene, with interaction lengths of 0.028%, 0.020%, and 0.061%, respectively. The carbon and copper targets were glued on the target supports made of paper ($C_6H_{12}O_6$) whose interaction length was 0.033%.

Tracking was performed with a cylindrical drift chamber (CDC) and a barrel-shaped drift chambers (BDC). The dipole magnet which had circular pole pieces of 880 mm in radius, provided the field integral of 0.81 Tm from the center to 1600 mm in radius where the BDC's were located.

For the electron identification the whole region of the electron arm was covered by two stages of electron identification counters. The first stage of the electron identification was done by front gas-Čerenkov counters (FGC) which covered from ±12 degrees to ±90 degrees horizontally and ±23 degrees vertically. The second stage consisted of three types of electron-identification counters. Rear gas-Čerenkov counters (RGC) covered ±12 degrees to ±54 degrees horizontally and ±6 degrees vertically. These regions corresponded to the kaon-arm acceptance. Rear lead-glass EM calorimeters (RLG) covered the same horizontal angle as RGCs, but vertically covered outside the kaon-arm acceptance, from ±5 degrees to ±23 degrees. In the backward region where the horizontal angle was larger than 57 degrees, the second-stage electron identification was done by side lead-glass EM calorimeters (SLG) which covered ±57 degrees to ±90 degrees horizontally and ±23 degrees vertically.

For the kaon identification, segmented aerogel Čerenkov counters and time of flight counters were used. The aerogel Čerenkov counters (AC) were a threshold-type Čerenkov detector using aerogel whose refractive index was 1.034, to separate kaons from pions in the momentum region of 0.53 to 1.88 GeV/c [25, 26]. Since we could not count beam protons particle by particle due to the high intensity, the event time-zero was given by the start timing counters (STC) placed at 380 mm from the targets. Forward time of flight counters (FTOF) were used to measure the time of flight of particles in the kaon acceptance. They were also used in combination with hodoscope counters (HC) to determine the charge and the crude momentum of the particles, and to make the kaon selection possible with the β (v/c) measurements in the trigger.

In the following section details of the experimental components are described.

2.2 Accelerator Facility and Beam Line

The proton synchrotron facility at KEK consists of four stages of accelerators, the 750 kV Cockroft-Walton, the 40 MeV LINAC, the 500 MeV Booster Synchrotron and the 12 GeV Proton Synchrotron (PS).

The typical beam intensity was 3×10^{12} in PS. During our experiment these protons were delivered to two beam lines simultaneously, about 1% to the EP1 beam line and remainder to EP2. The beam in EP1 can be switched either to EP1-A or to EP1-B. The beam line EP1-A is used for experiment using low energy kaons in the slow extraction mode and for the neutrino oscillation experiment in the fast extraction mode. The present experiment is located in EP1-B which is a special beam line for primary proton usage. The schematic view of the beam line EP1-B is shown in Figure 2.3.
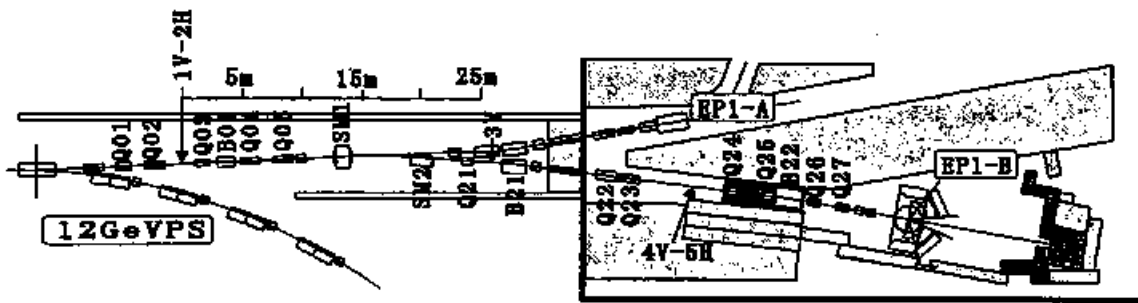

Figure 2.3: Schematic view of Beam Line(EP1B)

When EP1-B is in operation, protons extracted to the EP1 beam line were focused with a set of quadrupole magnets, Q01 and Q02 to the first vertical collimator 1V where the intensity was typically reduced to one-fifteenth. Here the initial image of the beam was defined by 1V together with the horizontal collimator 2H. At this point the beam spot from PS is vertically long so the beam intensity was controlled by changing the aperture of the collimator 1V Typical aperture of the collimators 1V and 2H were set as 6 mm and 2 mm respectively. Then the beam was bent by six degrees with the steering magnets SM1 and SM2, and was vertically focused with a set of

quadrupole magnets (**Q03, Q04, Q05, Q21**) to the point where the vertical collimator 3V was placed. The vertical collimator 3V was used to remove beam halo. Then the beam was transfered by the 'DQQ' (**B21, Q22, Q23**) complex to the first focusing point where the collimators 4H and 5V were located and again the rejection of beam halo was performed. After passing through the other beam-focusing complex 'QQDQQ' (**Q24, Q25, B22, Q26, Q27**), the beam was delivered to the final focusing point at the center of the spectrometer. At the target we obtained the size of the beam spot of 2∼3 mm in FWHM. At the end of the EP1-B beam line, the intensity of beam protons was monitored with 10% accuracy using an ionization chamber [27]. The repetition period was four seconds, and the flat top of the spill was about 1.7 seconds.

Prior to the experimental data accumulation, the aperture of the collimators were tuned to reduce the beam halo. It turned out that the adjustment of the collimators was effective to reduce the random trigger rate, so that the adjustment was done to minimize the interaction trigger rate with keeping the transmission of beam particles constant. The scanning of the magnetic field strengths of B21 and B22 was also effective to reduce the beam halo, by controlling the beam trajectory and minimize the interference of the beam halo with the beam pipe. We chose the setting where the least trigger rate was realized. The collimator settings in the present data-taking period are listed in Table 2.1.

1V	2H	3V	4V	5H
6 mm	2 mm	16 mm	20 mm	9 mm

Table 2.1: The collimator width setting

To estimate the number of triggered events which were not originated from interactions with the targets but from a chance coincidence or anything else, we removed the targets and collected no-target data. Typical fake trigger rates were found to be 78% in the electron first-level and 16% in the kaon first-level trigger.

2.3   The Spectrometer magnet

The spectrometer magnet was a dipole type with the overall weight of 300 ton. The dimension was 5655 mm in width, 3980 mm in height and 2120 mm in depth. To ensure the maximum vertical acceptance for electrons (± 23 degrees), the pole piece was made of two layers of cylinder with the diameters of 1760 mm and 2120 mm as shown in Figure 2.4. The gap between the poles was 907 mm. Other dimensions can be seen in Figure 2.4.

The magnetic field at the center of the pole piece was adjusted at 0.71 T to supply the integrated magnetic-field $\int B \cdot dl$ of 0.81 T·m from the targets to the radius of 1680 mm where the barrel drift chambers (BDCs) were located. The materials through the flight path of particles from the target to BDC are summarized in Table 2.2. By taking into account the typical position resolution of 350 μm of the chambers and the Coulomb scattering in the materials, the momentum resolution is given by the formula $(1.1 \times p \,[\text{GeV/v}] + 0.8)\%$. The first term is due to the position resolution of the chambers, and next term is due to the Coulomb scattering.

Since the amplitude of the $\int B \cdot dl$ is proportional to the rigidity of tracks, it is important to know the precise magnetic field-strength everywhere in the acceptance. The magnetic field map were obtained by the calculation and compared to the measurements. The magnet itself is symmetric from left to right, top to down and upstream to downstream. The actual field, however, was distorted due to other magnetic materials which were the ion plate on the floor to support the magnet weight and the magnetic shield placed just front of the photomultiplier tubes of the aerogel Čerenkov counter. We calculated the magnetic field map using the TOSCA [28], which is a finite element method program. All the magnetic materials were taken into account in the calculation. Since the preliminary calculations and the measurements proved the left-right symmetry of the field, we performed a full calculation assuming the left-right symmetry to reduce the calculation time. The strength of magnetic field on the x-y plane (the horizontal plane 400 mm below the beam line) is shown in Figure 2.5.

We measured the magnetic field (B_x, B_y, B_z) with a set of hall probes which were placed orthogonal to each other. The measured region was limited due to the technical limitation of the measurement device. We covered the region shown in Figure 2.6 with the 3-dimensional lattice points of 50 mm pitch. The three components of the magnetic field on the horizontal plane 363 mm below the beam line is shown in Figure 2.7.

Counter	material	position in radius [mm]	thickness X [mm]	λ_{rad} [mm]	X/λ_{rad} [%]
Target Chamber	helium	0.00	100.00	5281075.0	0.002
	Mylar	100.00	0.05	287.0	0.017
	air	100.05	279.95	304200.0	0.092
STC	scintillator	380.00	5.00	425.0	1.176
	lapping	385.00	0.20	287.0	0.070
	air	385.20	14.80	304200.0	0.005
CDC	Mylar	400.00	0.05	287.0	0.017
	$Ar\text{-}C_2H_6$(50:50)	400.05	479.95	340350.0	0.141
	Wire (Cu-Be)	-	0.031	14.3	0.217
	Wire (W)	-	0.0005	3.5	0.014
	Mylar	880.00	0.05	287.0	0.017
	air	880.05	19.90	304200.0	0.007
FGC	Mylar	899.95	0.05	287.0	0.017
	isobutane	900.00	660.00	169300.0	0.390
	acrylic mirror	1560.00	3.00	344.0	0.872
	aluminum cover	1563.00	1.00	89.0	1.124
	air	1564.00	5.95	304200.0	0.002
BDC	Mylar	1569.95	5.95	287.0	0.017
	$Ar\text{-}C_2H_6$(50:50)	1570.00	110.00	340350.0	0.032
	Wire (Cu-Be)		0.010	14.3	0.070
	Wire (W)		0.0001	3.5	0.003
SUM					4.303

Table 2.2: List of the materials and their radiation lengths from the center of CDC to the radius of 1680 mm where BDCs were located.
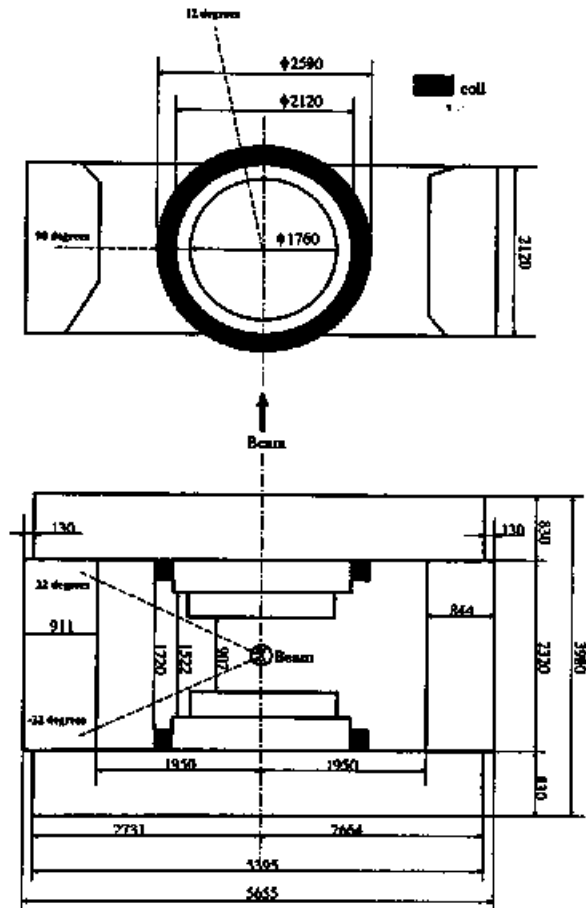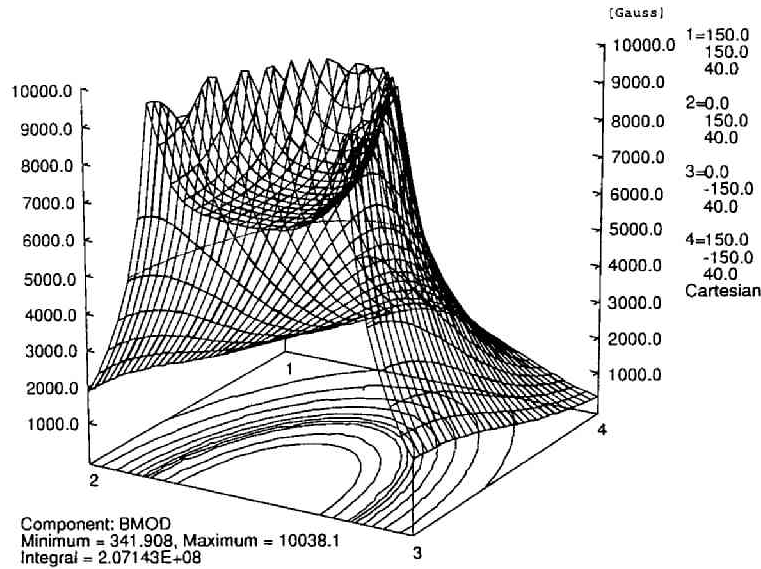
Figure 2.4: Schematic view of the spectrometer magnet. The dashed lines indicate the electron acceptance.

[Gauss]

10000.0
9000.0
8000.0
7000.0
6000.0
5000.0
4000.0
3000.0
2000.0
1000.0

1=150.0
150.0
40.0

2=0.0
150.0
40.0

3=0.0
-150.0
40.0

4=150.0
-150.0
40.0
Cartesian

Component: BMOD
Minimum = 341.908, Maximum = 10038.1
Integral = 2.07143E+08

Figure 2.5: The calculated magnetic field map(z = -400mm)

We evaluated the systematic uncertainty of the momentum determination caused from the inaccuracy of the magnetic field map. We generated the drift chamber hits points associated with the charged particle trajectories which were generated with the measurement map, and we fitted them using the Runge-Kutta method with the calculated map. By comparing the original momenta with the fitted results, we found that the discrepancy was within $0.2\% \pm 0.3\%$ in the momentum region from 0.5 GeV/c to 2.0 GeV/c. as shown in Figure 2.8. The systematics is small enough compared with the momentum resolution which will be given in Section 3.3.3.

2.4 Targets and Target Chamber

We used three kinds of targets aligned in-line, carbon, polyethylene and copper. The interaction length and radiation length of the targets used in the present experiment are summarized in Table 2.3. These targets were placed at the center of the cylindrical drift chamber (CDC) by 44 mm apart from each other. The schematic view of the target holder is shown in Figure 2.9. The targets were held at the bottom sandwiched by the two polyethylene
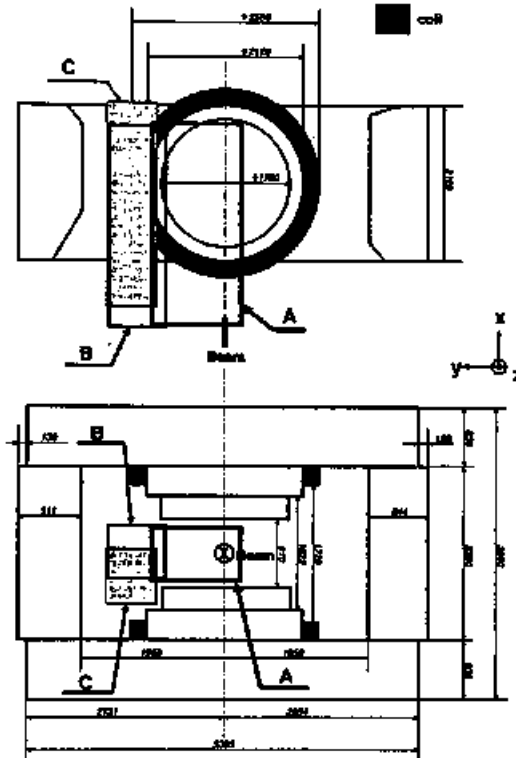
Figure 2.6: The region of magnetic field measurement.

material		mass number	thickness [mg/cm^2]	interaction length[%]	radiation length[%]
polyethylene	CH$_2$		47.8	0.061	0.107
carbon	C	12.011	24.3	0.028	0.057
copper	Cu	63.546	26.8	0.020	0.199
paper	-[C$_6$H$_{10}$O$_5$]-		28	0.033	0.055

Table 2.3: The interaction length and radiation length of the nuclear targets used in the experiment
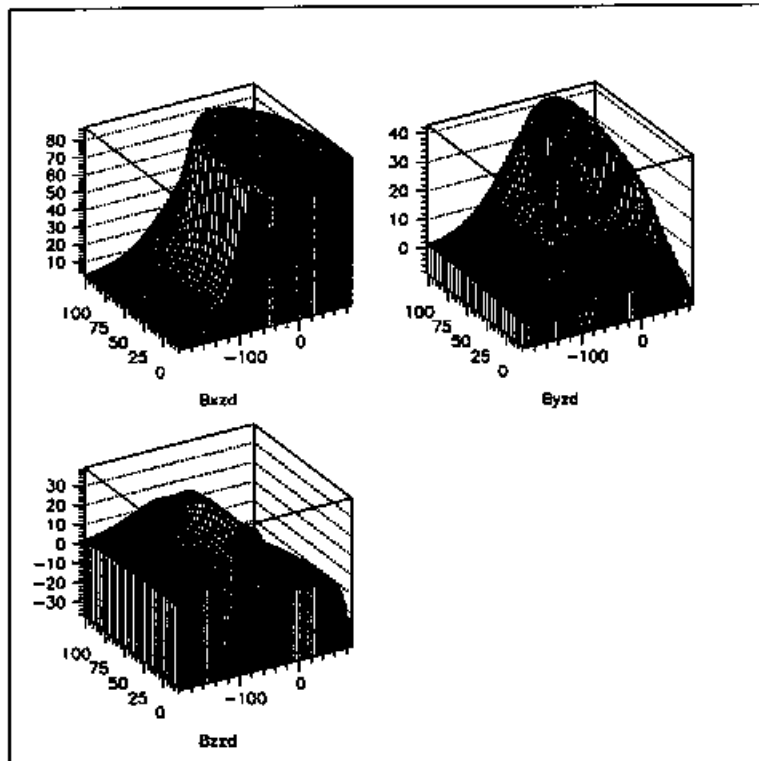
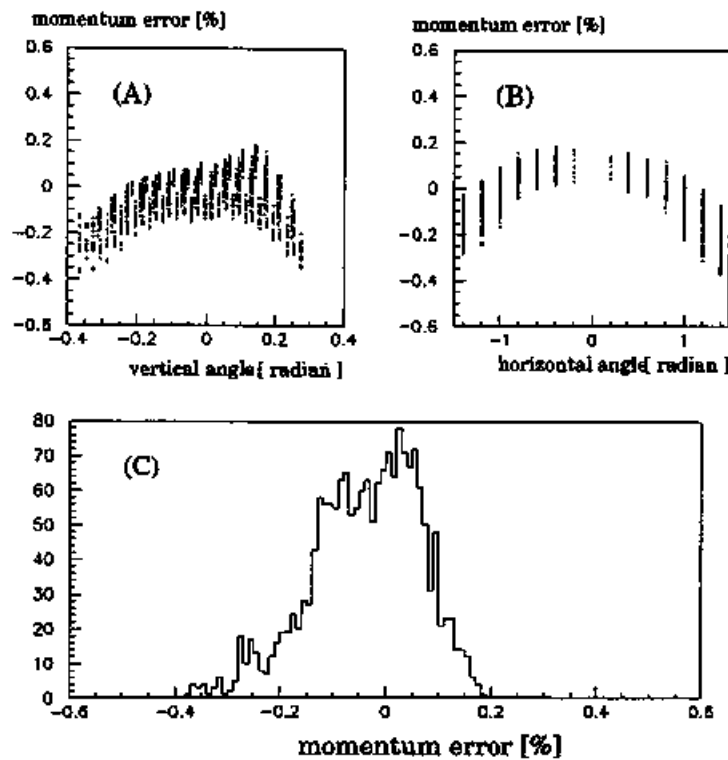Figure 2.7: The measured magnetic field map(z = -363 mm)

Figure 2.8: Possible uncertainty of the momentum determination due to the magnetic field map. Test tracks were generated with the measured map and reconstructed with the calculated map. The differences of the reconstructed momenta from the generated momenta were plotted as a function of the vertical angle in (A), and the horizontal angle in (B). The histogram (C) gives the projection of all the ratios.
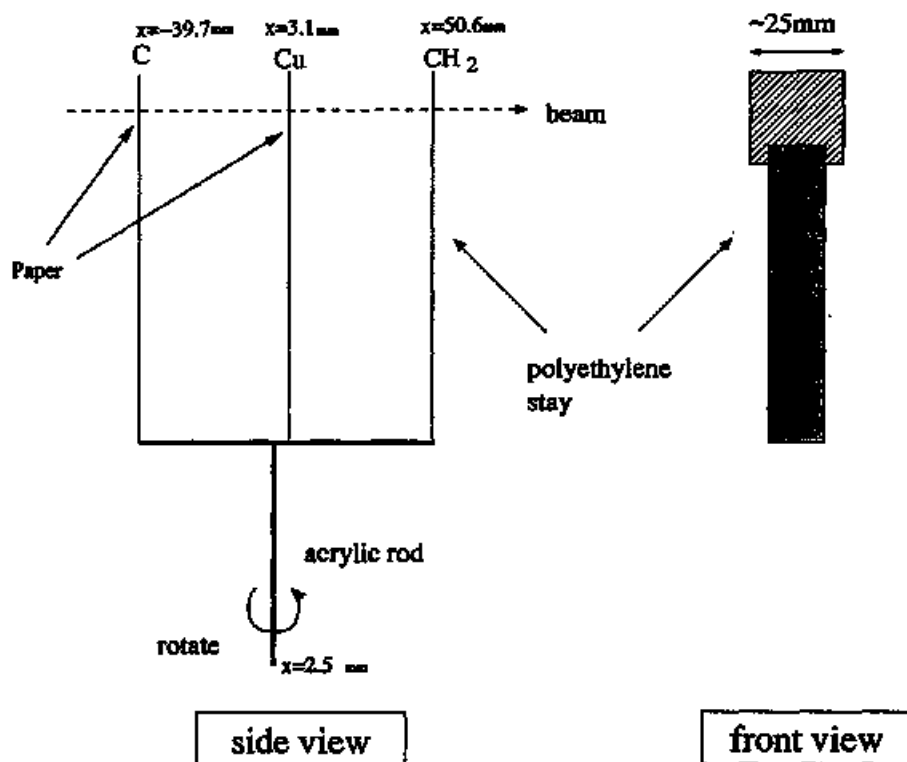
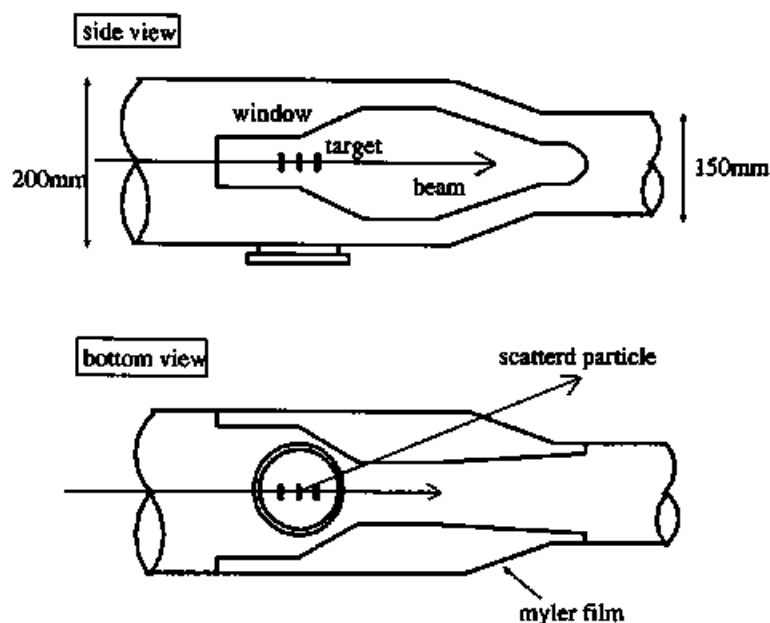Figure 2.9: Schematic view of Target

Figure 2.10: Schematic view of Target and Target chamber

stays with a thickness of 1 mm. The target holder was rotated by 180 degrees along the z-axis in every 12 hours to minimize the position dependence of the acceptance for each target position. The target x-positions with respect to the center of CDC were -39.7 mm for carbon, 3.1 mm for copper and 50.6 mm for polyethylene when the carbon target was located upstream.

To decrease the interaction of beam protons with air, the entire beam line was kept as vacuum from the extraction point to an exit of **Q27**, the last beam line magnet of EP1B. At the exit of **Q27**, the region of vacuum was terminated with a 200-μm-thick Mylar sheet and was fllowed by a helium-filled beam pipe. A helium gas was folowed at a rate of 1000 cc per minute. The pipe was directly connected to the target chamber which is shown in Figure 2.10. The length of the helium-filled region was 4.6 m from **Q27** to the target position.

The target chamber was made of 5 mm-thick aluminum with the windows covered with 50-μm-thick Mylar sheets for the outgoing particles into the detector acceptance. Downstream the target chamber, a helium-filled beam pipe of 5.5 m long followed.

2.5 Tracking

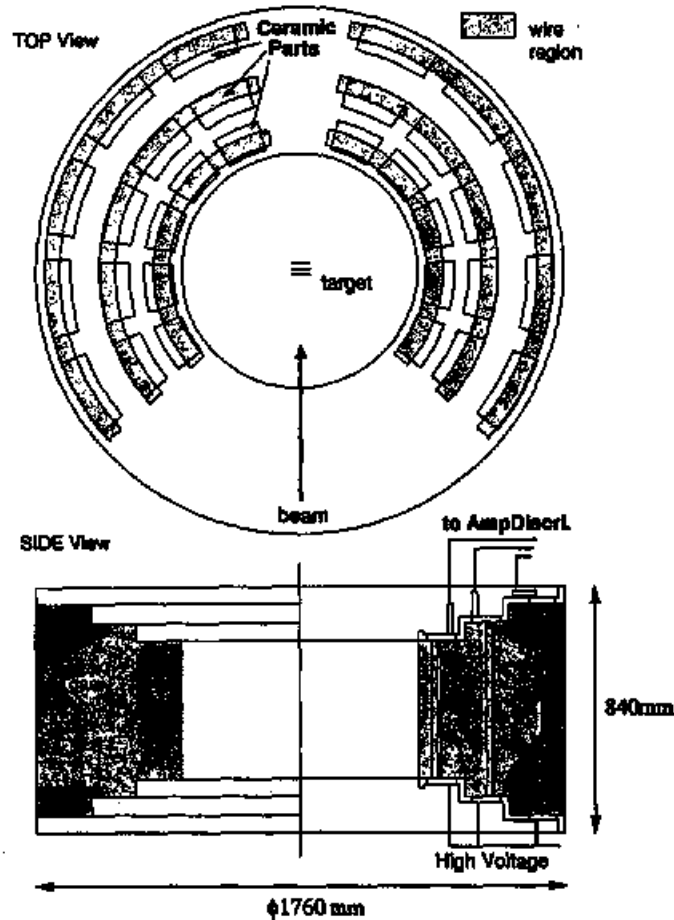### 2.5.1 Cylindrical Drift Chamber

Figure 2.11: Schematic view of CDC

The schematic view of the Cylindrical Drift Chamber (CDC) is shown in Figure 2.11. The outer diameter of CDC is 1760 mm, the inner diameter is 800 mm and the height is 840 mm. We located CDC on the pole piece of the spectrometer magnet. The acceptance of CDC was from ±12 degrees to ±132 degrees horizontally and ±22 degrees vertically.

The CDC consists of ten radial layers of the drift cells, and they were

grouped into three super-layers. The first super-layer was in the radial region from 445.0 to 475.0 mm having three layers of drift cells (X, X', U), the next was from 602.5 to 642.5 mm having four layers (V, V', X, X'), and the last was from 800.0 to 830.0 mm having three layers (U, X, X'). In the X and X' layers the direction of wires was vertical and in the U and V layers the wires were tilted by about ± 0.1 radian. Argon-ethane mixed gas of 50% and 50 % was used at 1 atm.

The structure of the drift cells is shown in Figure 2.12. All the drift cells of CDC had the same horizontal angular coverage of 1.5 degrees with respect to the targets. For the most-inner super-layer, the high voltage of -2.1 kV was applied to the potential wires and of -1.37 kV to the guard wires. For the next super-layer, the high voltages of -2.2 kV and -1.43 kV were applied to the potential and guard wires, respectively. For the most-outer super-layer, the same high voltages were applied to the wires. The sense wires were kept at the ground level. Details of the wire arrangements were shown in Table 2.4.

layer number	1	2	3	4	5	6	7	8	9	10
wire direction	X	X'	U	V	V'	X	X'	U	X	X'
radial location of the sense wire [mm]	445	455	475	602.5	612.5	632.5	642.5	800	820	830
cell width [degree]	1.5	1.5	1.5	1.5	1.5	1.5	1.5	1.5	1.5	1.5
cell width [mm]	11.65	11.91	12.43	15.77	16.04	16.55	16.82	20.94	21.47	21.73
tilt angle [radian]	0	0	0.1127	0.1116	0.1135	0	0	0.1174	0	0
number of sense wires	81	81	77	76/77 (*)	77/76 (*)	81	81	77	82	82

(*)left-arm and right-arm

Table 2.4: CDC wire configuration.

We calculated the electrical field shape of the chamber cell and the relation between the drift length and the drift time with the drift chamber simulation code Garfield [29]. The simulated drift line in the outer super-layer is shown in Figure 2.13 and the relation between the drift length and the drift time (x-t relation) is shown in Figure 2.14. The obtained x-t relation
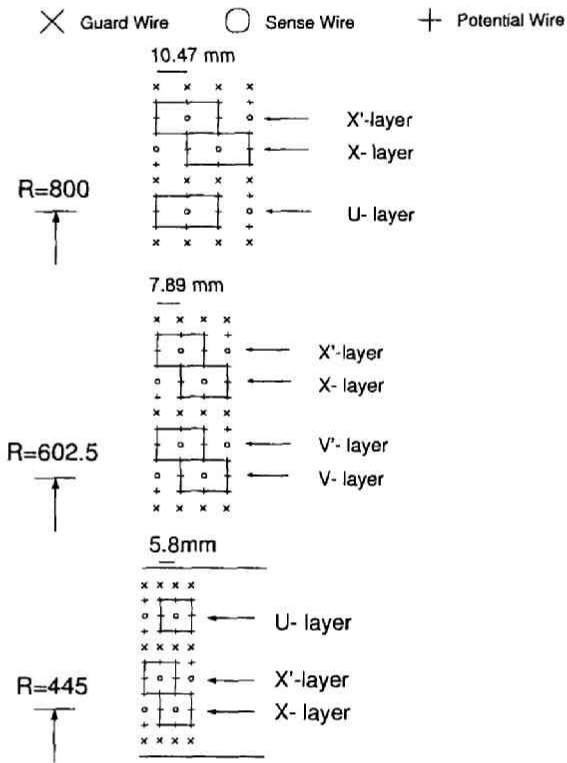
Figure 2.12: The cell structure of CDC

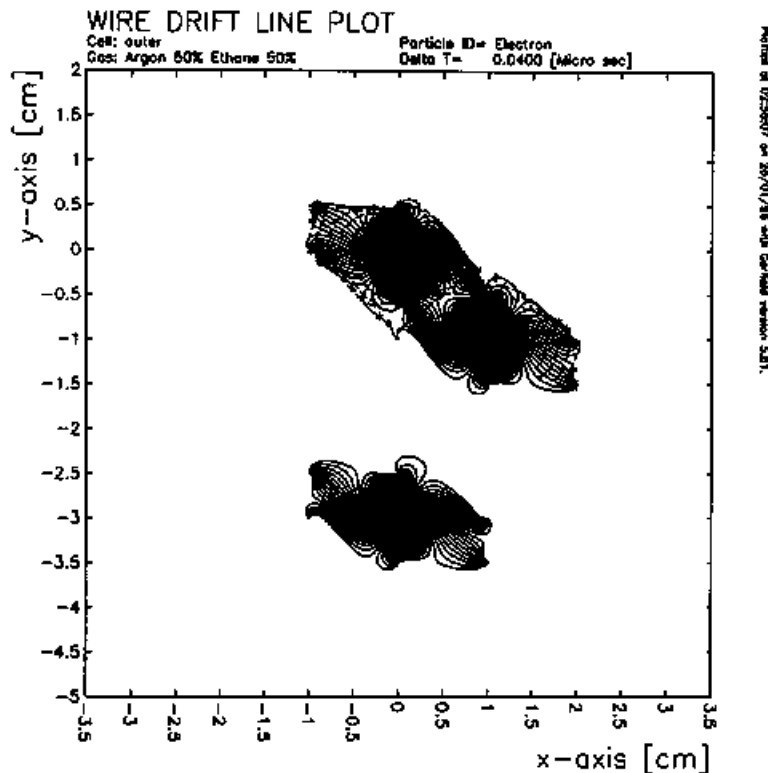was used to determine hit positions after the adjustment to the real data.

Figure 2.13: The simulated drift line in the outer super-layer (3 layers) in the magnetic field of 0.61T, which corresponds to the magnetic field at this point when the spectrometer magnet is fully excited.

The structure of CDC was designed to restrict its active region only to the spectrometer acceptance. The top and bottom end plates were semi-curved with 3 stages as shown in Figure 2.11. This structure was effective to gain the mechanical strength and then to minimize the support structure within the spectrometer acceptance.

The end plates and the support structure of CDC was made of aluminum. Thirty ceramic plates were mounted on the aluminum end plates as shown in Figure 2.11 and Figure 2.15. The ceramic plates had an print-circuit pattern which provided electrical connections to the feedthrough pins as shown in Figure 2.16. The feedthroughs were made of gold plated brass of a 1.8 mm diameter pipe. To secure the electrical connection a cut-ring spring was
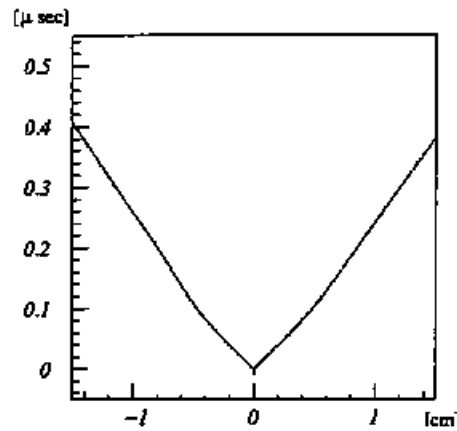
Figure 2.14: The calculated relation between the drift time and the drift length of the X-layer in the outer super-layer under the magnetic field of 0.61T

inserted between the feedthrough and the through hole. The ceramic board on the top provided the signal connections to the sense wires and these on the bottom provided the high voltage connections. The ceramic boards were 100mm in width, 200mm in length and 20mm in thickness and located precisely on the end plates by the knock pins with the machining precision of about 10 μm. In-between the ceramic board there were the ribs of the aluminum end plate, where the feedthroughs made of Delrin as shown in Figure 2.17 were used.

The sense wires were gold-plated tungsten of 30 $\mu m\phi$ and the potential wires were Be-Cu of 100 $\mu m\phi$. The position of the wire was determined by the bush inserted at the end of the feed through pipes. We used the bush with a 80 $\mu m\phi$ hole for the sense wires, so that the precision of the wire positioning was about 25 μm.

The read-out electronics of CDC consisted of pre amplifier, post amplifier, discriminator and time to digital converter (TDC). The pre-amplifiers were mounted on CDC. The Radeka type pre-amplifiers, which were charge sensitive bipolar amplifiers with the gain of 200 mV/pC, were used. The electric circuit of the Radeka type pre amplifier is shown in Figure 2.18 [30]. The output signals of the pre amplifier were sent to the post amplifier via 10m-long twisted-pair cables. The gain of the post amplifier was 10 and output was discriminated to the ECL logic signal and transfered to the counting
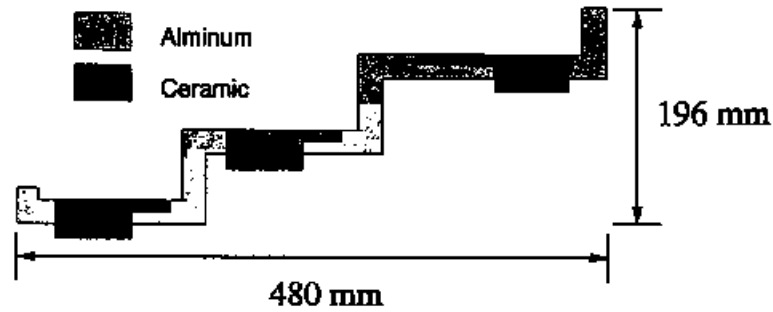
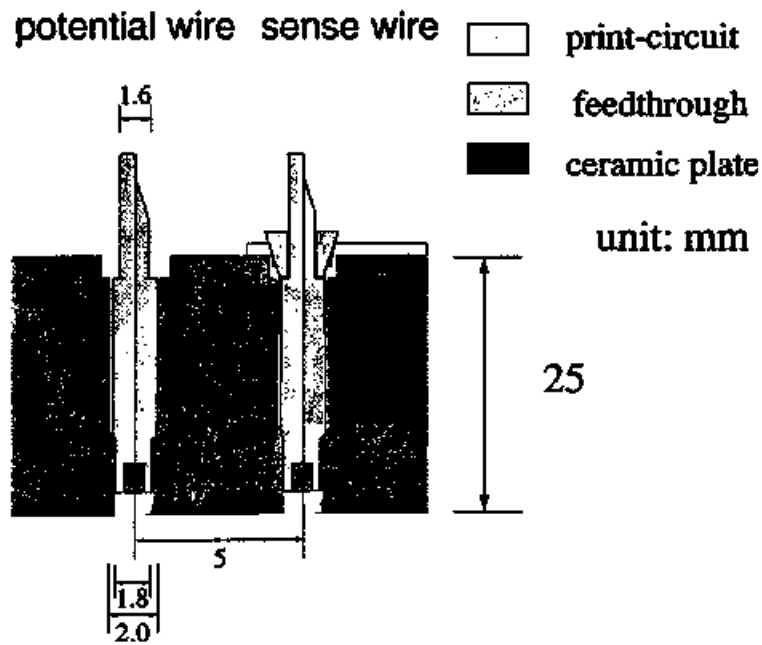Figure 2.15: The cross section of the aluminum end plate and the ceramic plate

Figure 2.16: Schematic view of the feedthrough structure for the ceramic plate of CDC
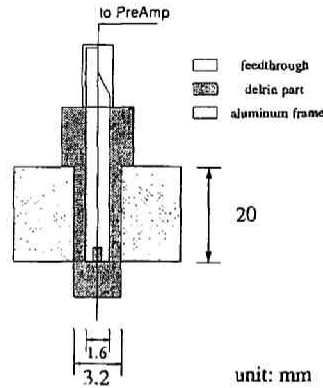
Figure 2.17: Schematic view of the feedthrough structure for the aluminum plate of CDC

house via 50m-long twisted-pair cables.

When a minimum ionizing particle passed through one drift cell of CDC, it generated about 100 ionizing electrons. The electric field around the wire amplified these electrons by 1.6×10^4 Thorough the pre- and post-amplifiers, the pulse hight of the signals before the discriminator was typically 500 mV for minimum ionizing particles. The threshold voltage of the discriminator was set at 35 mV

2.5.2   Barrel-shaped Drift Chambers

The structure of Barrel-shaped Drift Chambers (BDC) consisted of 90-degrees arc-shaped end plates at the top and the bottom which were supported by 3 aluminum bars as shown in Figure 2.19. The inner radius was 1570 mm, the outer radius was 1680 mm and the height was 1420 mm. The acceptance of BDC is the same as CDC for the vertical coverage but with a smaller horizontal coverage from ± 7.5 degrees to ± 94.5 degrees. The BDC's have 4 layers of drift cells with an XX'UV configuration, located at r=1600 to 1650 mm. In the X and X' layers the direction of wires was vertical and in the U and V layers the wires were tilted by about $\pm$ 0.1 radian. As CDC argon-ethane mixed gas of 50% and 50 % was used at 1 atm.

The structure of the drift cells is shown in Figure 2.20. All the drift cells of BDC had the same horizontal angular coverage of 0.75 degrees with respect to the target position. The size of the drift cells of BDC was the
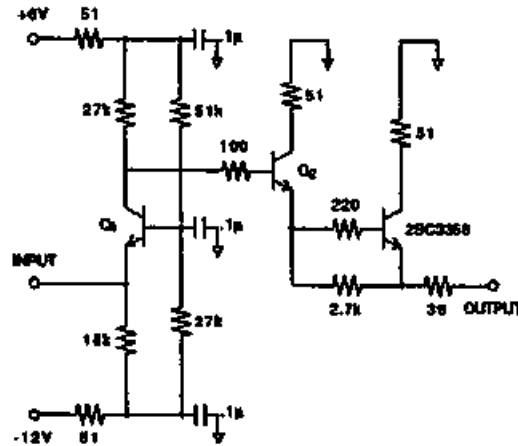
Figure 2.18: The electric circuit of the Radeka type pre-amplifier.

same as that of the outer super layer of CDC. The high voltage of -0.7 kV was applied to the potential wires, of +0.1 kV to the guard wires and of +1.5 kV to the sense wires. Details of the wire arrangements were shown in Table 2.5.

layer	1	2	3	4
wire direction	X	X'	U	V
location of sense wire	1600	1610	1630	1650
from the center of the arc [mm]				
cell width [degree]	0.75	0.75	0.75	0.75
cell width [mm]	20.81	20.94	21.21	21.47
tilt angle [radian]	0	0	0.1058	0.1071
number of sense wire	116	116	109	109

Table 2.5: BDC wire configuration.

The read–out electronics of BDC were the same as that of CDC and the threshold voltage of the discriminator was set at 75 mV
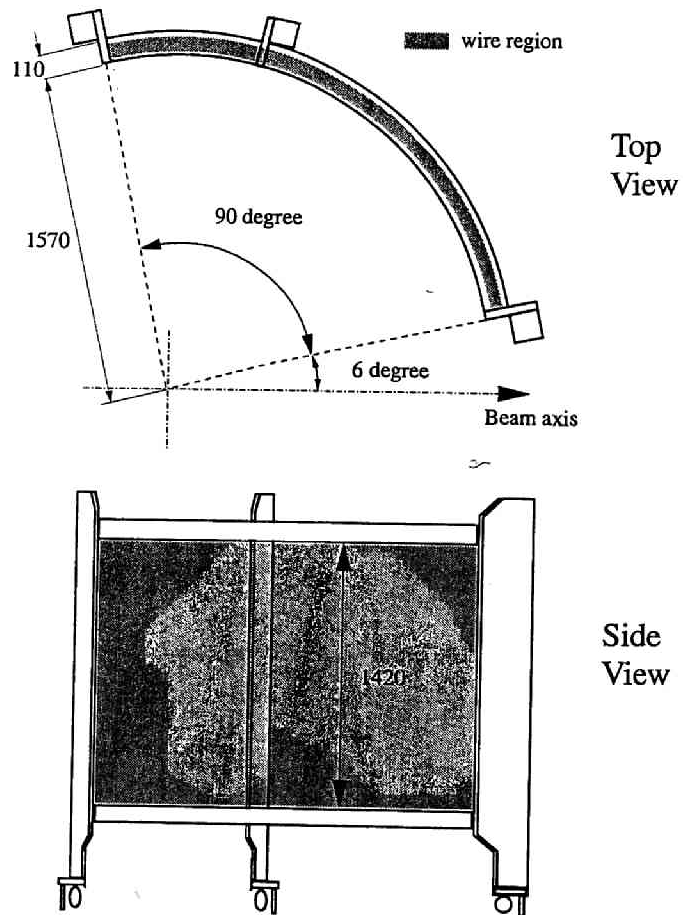
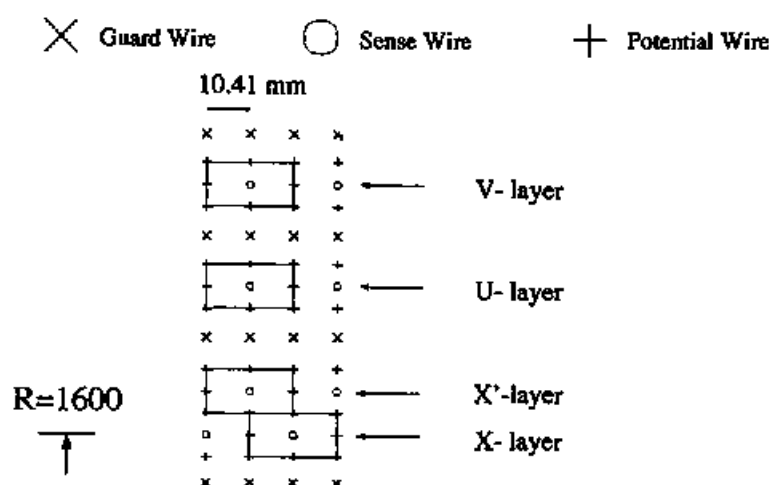Figure 2.19: Schematic view of BDC

Figure 2.20: The cell structure of BDC

2.6 Electron Identification Counters

2.6.1 Start Timing Counter

The time zero of an event was defined by the start timing counters (STC), since we could not count the beam protons one by one because of their high rate ($\sim 7 \times 10^8$ protons per second). We located STC at 380mm from the center of the spectrometer, covering from ± 12 to ± 60 degrees in the horizontal angle and ± 23 degrees in the vertical angle. In each arm STC was segmented into 8 units horizontally.

The scintillator of STC was made of Bicron BC404. The dimension of the scintillator segment was 400 mm in height, 40 mm in width and 3 mm in thickness. The scintillation light was transfered through light guides to a pair of photomultipliers attached at the top and bottom ends. The photomultipliers were H6154 of Hamamatsu Photonics, whose diameter of the photocathode was 2 inches and structure of the dynodes was a fine-mesh type. They could be operated under the magnetic field of 0.71T. The number of dynodes was 19 with the typical gain of 1×10^6 at this field strength. Since the coincidence rate of the top and bottom photomultipliers reached 1M counts per spill in the forward segments, the high voltage breeder was modified to supply enough current to the last three dynodes. The breeder circuit is shown in Figure 2.21. Typical breeder current was 0.4 mA which

was increased to 4 mA at the last three dynodes. Discriminated signals from the top and bottom photomultipliers were fed into the mean timer and provided the timing of the segment. The timings of all the STC segments were adjusted within 1 nsec. These signals were OR-ed and used as the event time-zero signal.

2.6.2 Front Gas-Čerenkov Counter

The front gas-Čerenkov counters (FGC) covered from ± 12 degrees to ± 90 degrees horizontally and ± 23 degrees vertically. They were horizontally segmented into 13 units in each arm so that one segment covered 6 degrees. The cross section of FGC is schematically shown in Figure 2.22, together with the light collection scheme.

Iso-butane gas with refractive index of 1.0019 was used as the Čerenkov photon radiator. The threshold momentum for pions is 2.3 GeV/c. Since the path length of particles in the counter was rather short, we used the gas having high refractive index. Another merit of iso-butane was its transparency for the ultra-violet lights down to the wave length of 220 nm. It is important for the detection of the Čerenkov light because the intensity of Čerenkov light is higher at a short wavelength with a $1/\lambda^2$ dependence.

A radiated Čerenkov photons were reflected twice on the flat and the arc mirrors. To suppress multiple scattering, it was required to use thin mirrors. For the flat mirror we used 0.05 mm aluminized Mylar supported with a honeycomb backplane made of paper. The arc mirrors were made by a 3 mm-thick Acrylic plastic on which aluminum and SiO were successively evaporated. Light is reflected also at the walls for the segmentation. We used MgF_2-coated aluminized Mylar which has 88% reflectance for the wave length down to 200 nm.

The Čerenkov photons were focused with a Winston funnel [31] attached on the photomultipliers. Since the photomultipliers of FGCs were operated under the magnetic field of about 0.2T, we used R5542 of Hamamatsu Photonics which had 19 stages of fine-mesh dynodes. For the detection of Čerenkov photons, their window was made of UV-transparent glass with a diameter of 3 inches.

We tested a 1/2 sector model with no magnetic field. The vertical and horizontal incident angle dependence of the efficiency and the average number of photo-electrons were obtained using 500 MeV/c electron. The results are summarized in Figure 2.23 and 2.24. We obtained more than 5 photo-
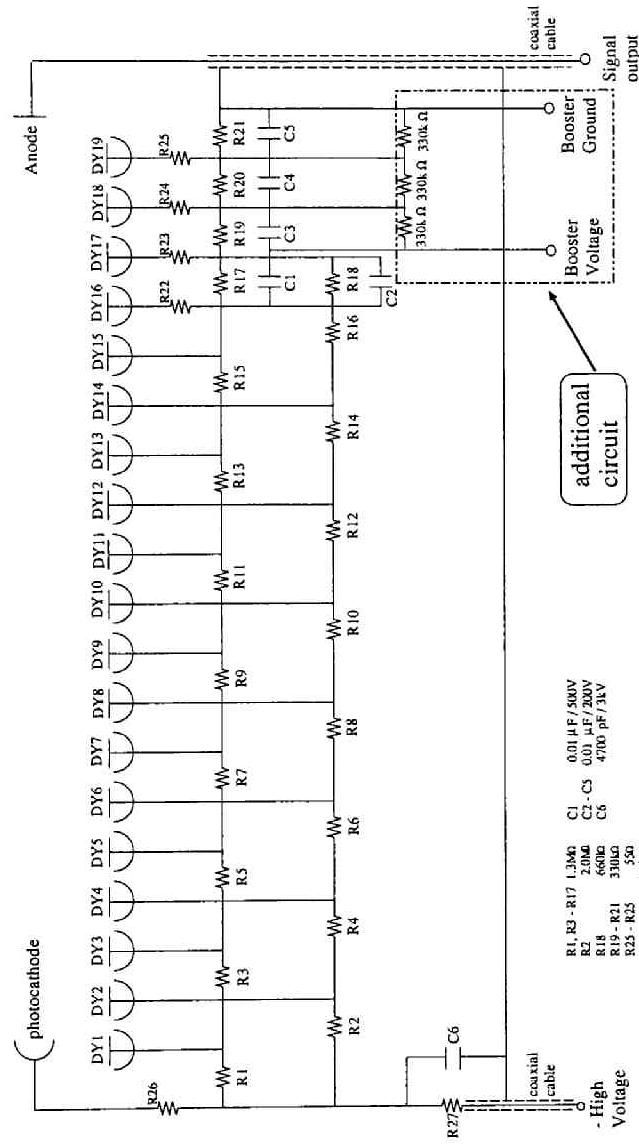
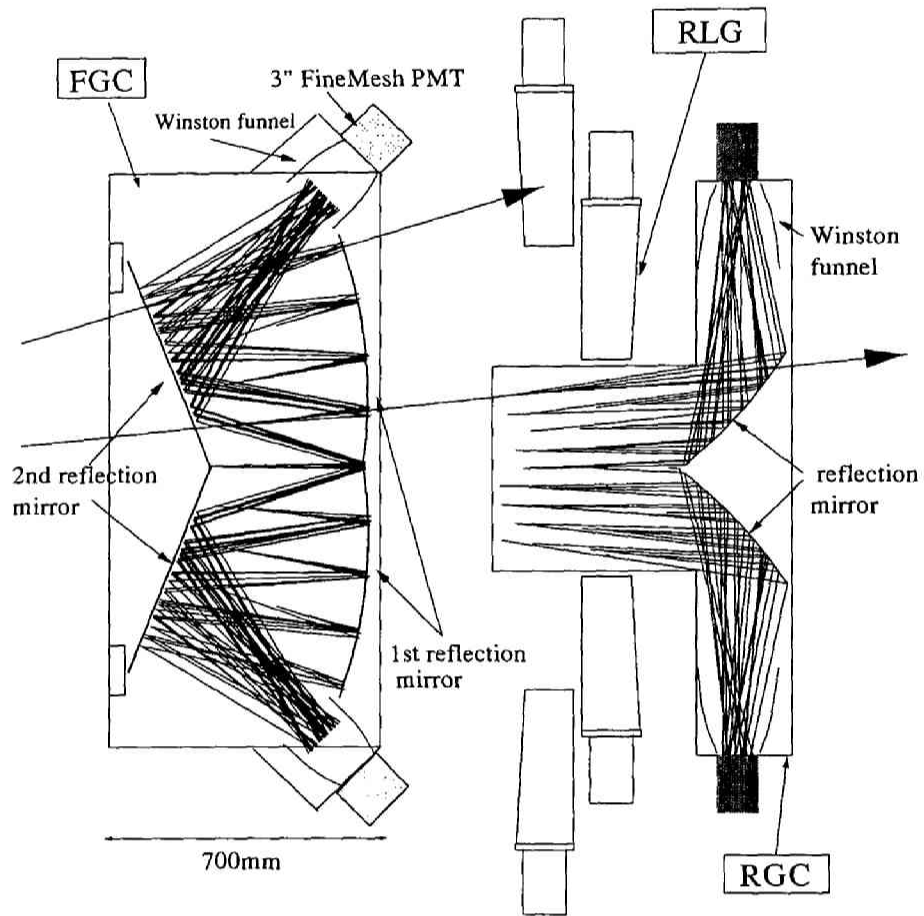Figure 2.21: The breeder circuit of the photomultiplier used for STC (Hamamatsu H6154).

Figure 2.22: Schematic view of FGC,RGC and RLG

electrons in all the region required for the spectrometer. Please note that with the horizontal angle more than 0.15 radians the electrons pass more than 1 segment so that the pulse from the neighbor segment must be added. The horizontal incident angle of 0.2 radian corresponds to the momentum of 400 MeV/c. The photo-electron distribution for 500 MeV/c π mesons is also shown in Figure 2.25. We calculated the rejection power as the ratio of the number of π mesons, which produced more than 1 photo-electron, over all π mesons. From the result of calculation the rejection power was 0.8×10^{-2} This rejection power was not achieved in the physics data taking. Details are described in Section 3.3.6.

2.6.3   Rear Gas-Čerenkov Counter

The rear gas-Čerenkov counters (RGC) which covered ± 12 degrees to ± 54 degrees horizontally and ± 6 degrees vertically with 7 horizontal segments in each arm. These regions corresponded to the kaon-arm acceptance. The cross section of RGC is schematically shown in Figure 2.22, together with the light collection scheme.

Iso-butane gas was used for the radiator as FGC. A radiated Čerenkov photons were reflected once on the arc mirror which was made by the 3 mm thick Acrylic plastic on which aluminum and SiO were evaporated. Light is reflected also at the walls for the segmentation. The photons were focused with a Winston funnel [31] attached on the photomultipliers. We used R1652 of Hamamatsu Photonics with a diameter of 3 inches.

We tested a 1/2 sector model with no magnetic field. The vertical and horizontal incident-angle dependence of the efficiency and the number of mean photo-electron were obtained using 1.0 GeV/c electron as summarized in Figure 2.26 and 2.27. We obtained the number of photo-electrons of more 3 for the acceptance required for the spectrometer. The lower number of photo-electrons at 0.025 radian (Figure 2.26) was attributed to the acceptance of the 1/2 module. The photo-electron distribution for 1 GeV/c π mesons is also shown in Figure 2.28. We calculated the rejection power same as FGC, the result was 3.9×10^{-2}

2.6.4   Rear Lead-Glass EM Calorimeter

The rear lead-glass EM calorimeters (RLG) covered the same horizontal angle as RGCs with 12 segments in each arm, but vertically covered outside the
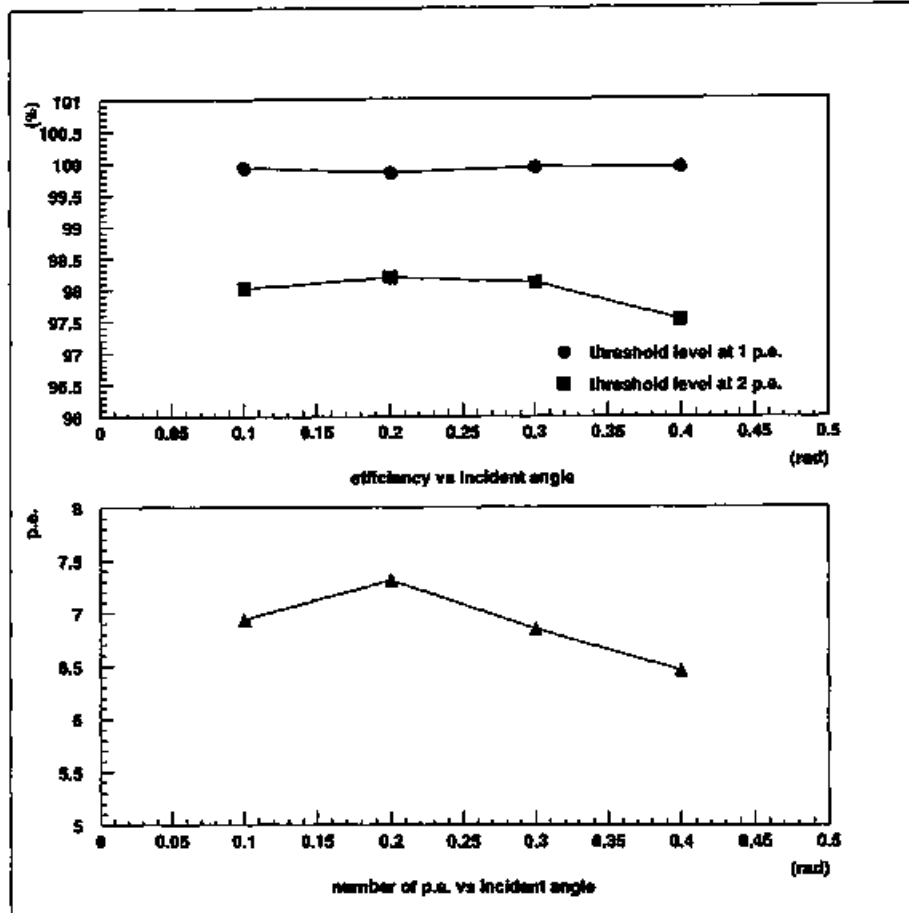
Figure 2.23: The efficiency and the number of photo-electron (mean) of the FGC test module as functions of the vertical angle of incident electrons. The triangles show the number of photo-electrons and the circles and the rectangles show the efficiency for the threshold levels corresponding to 1 photo-electron and 2 photo-electrons, respectively.
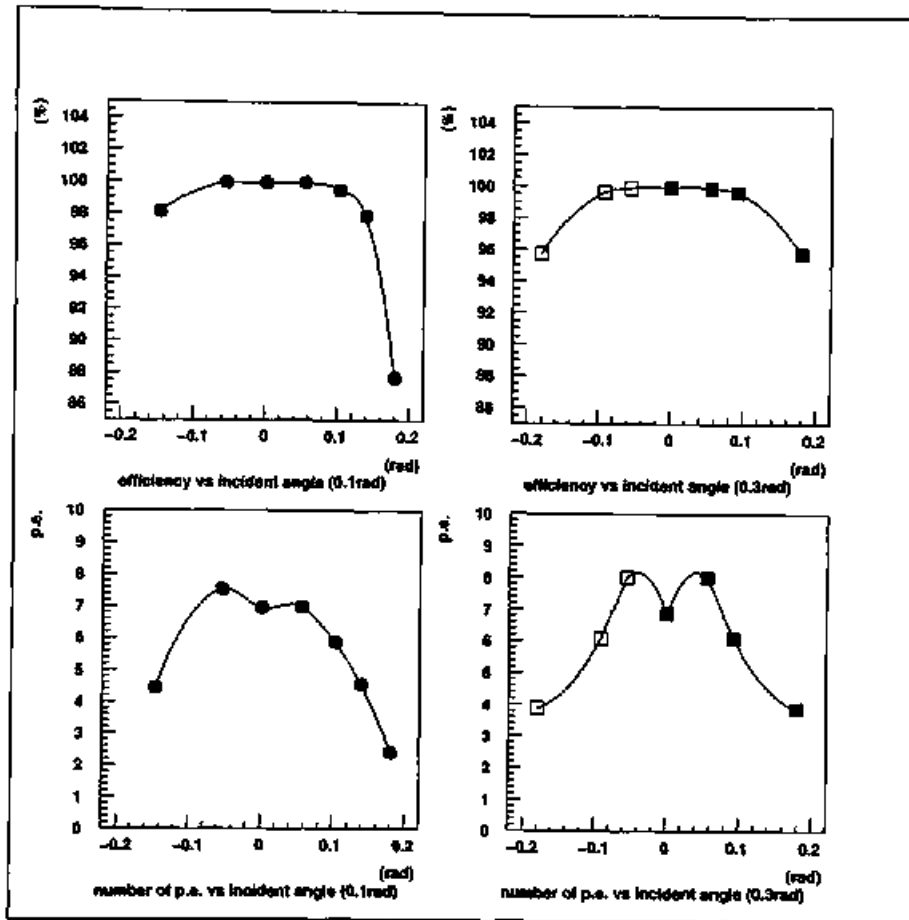
Figure 2.24: The efficiency (upper figures) and the number of photo-electron (lower figures) of the FGC test module as function of the horizontal angle of incident electrons. The closed circles are the data for the electrons with the vertical angle of 0.1 radian and the closed rectangles of 0.3 radians. The open rectangles are the points added assuming the symmetry.
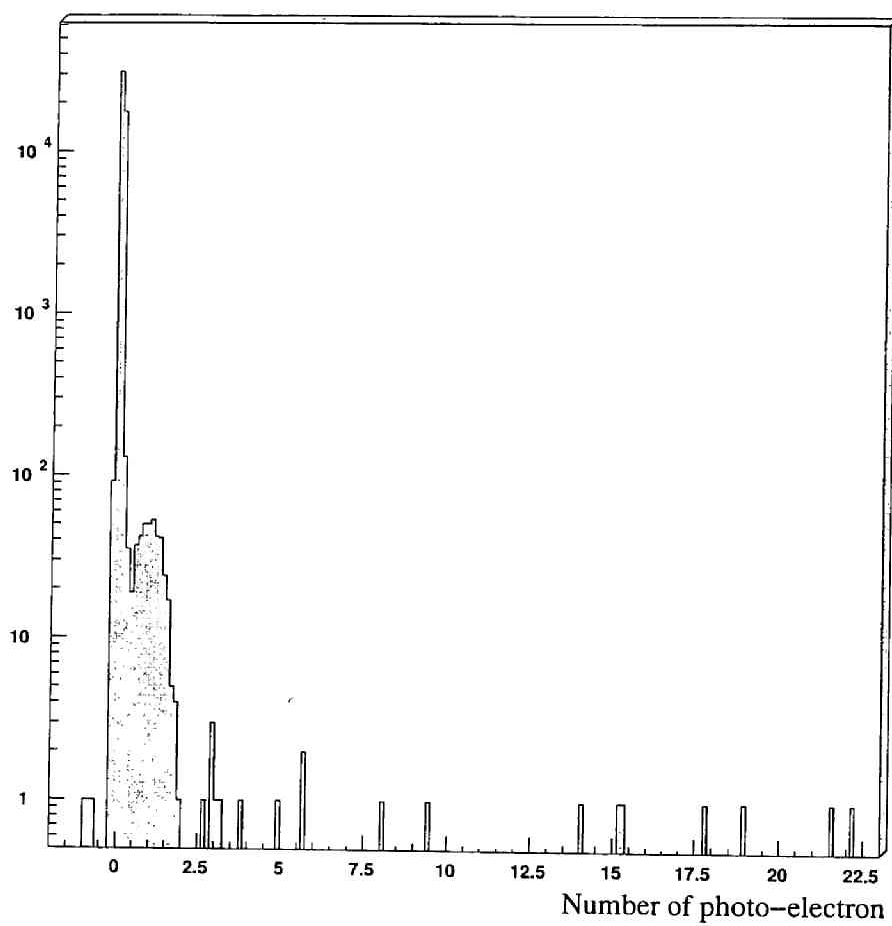
Figure 2.25: The photo-electron distribution of FGC for 500 MeV/c π mesons.
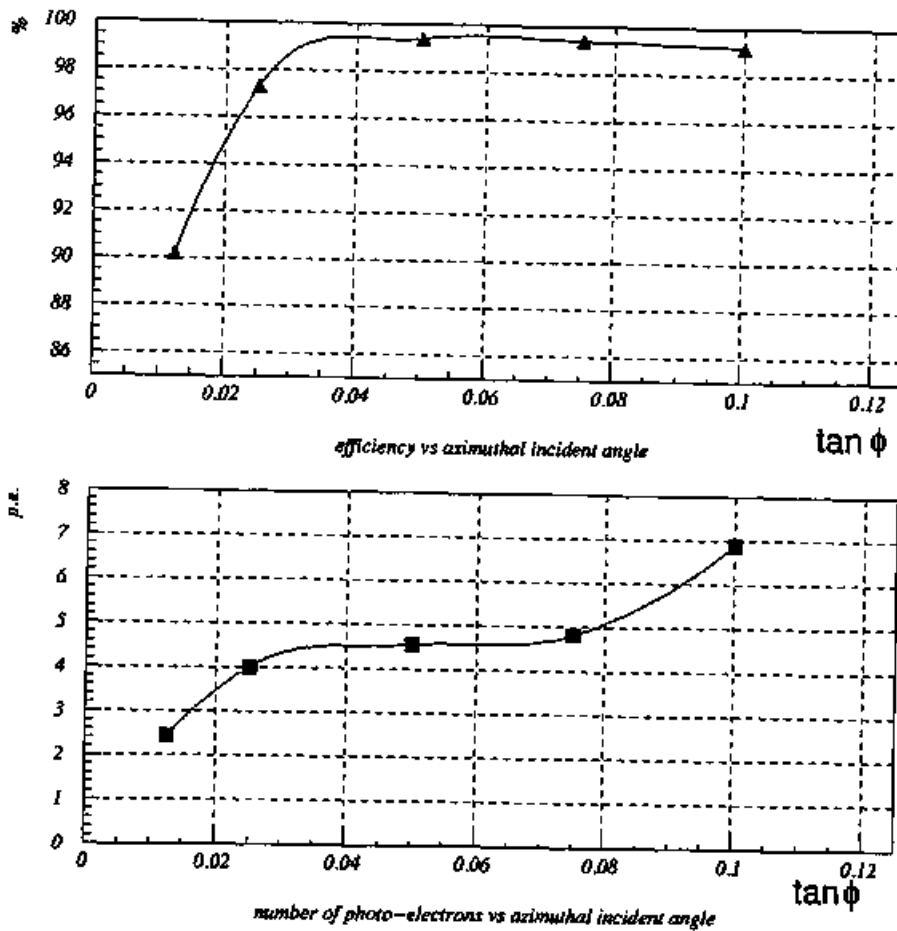
Figure 2.26: The efficiency (top figure) and the number of photo electron (bottom figure) of the RGC test module as functions of the vertical angle of incident electrons.
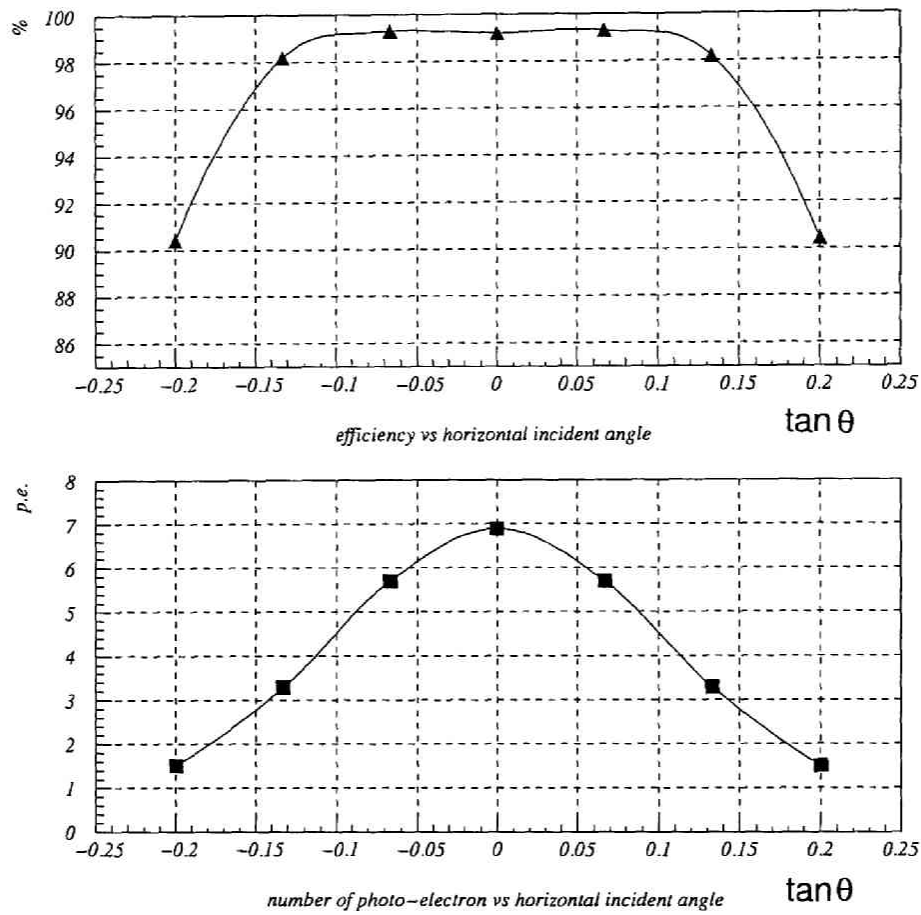
Figure 2.27: The efficiency (top figure) and the number of photo electron (bottom figure) of the RGC test module as function of the horizontal angle of incident electrons.
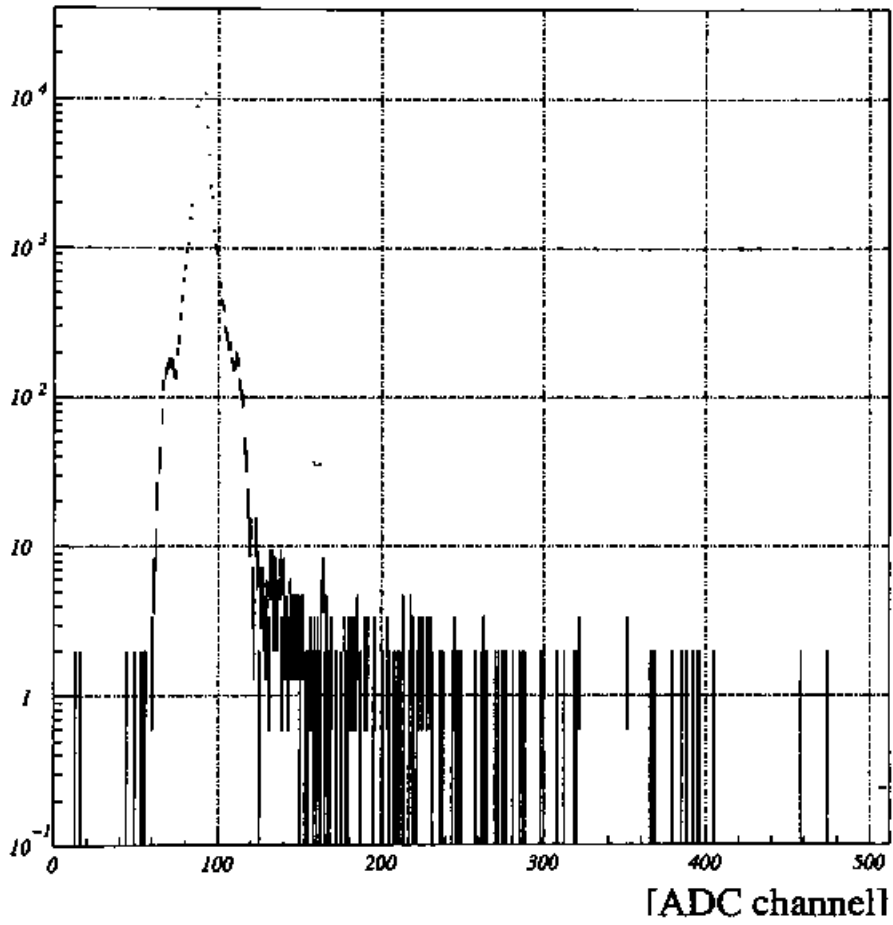
Figure 2.28: The ADC spectra of RGC for 1 GeV/c π mesons.

kaon-arm acceptance, from ±5 degrees to ±23 degrees.

RLG consisted of SF6W lead-glass block, which had the size of 33 cm height, 12 cm width and 11 cm thickness. These blocks recycled from the EM calorimeter of TOPAZ of TRISTAN at KEK. The lead glass blocks were used as they were but with a different arrangement as shown in Figure 2.22. To cover a large region with the small number of segments, such unusual arrangements were adapted. Čerenkov photons from an EM shower were transported vertically by the total reflection to the photomultipliers at the end of the block. The PMTs R1652 of Hamamatsu Photonics with a diameter of 3 inches were used.

2.6.5 Side Lead-Glass EM Calorimeter

In the backward region where the horizontal angle was larger than 57 degrees, the second-stage electron identification was done by the side lead-glass EM calorimeters (SLG) which covered ±57 degrees to ±90 degrees horizontally and ±23 degrees vertically with 9 horizontal segments in each arm. The cross section of FGC and SLG is schematically shown in Figure 2.29.

We reuse the TRISTAN lead glass carolimeter blocks same as RLG. For SLG, we reshaped and repolished the blocks in Tochigi Nikon Corporation into a rectangular shape from the original tapered shape, and five units of the lead-glass blocks were stacked vertically and glued epoxy resin to form one segment of the calorimeter. The one segment of SLG had the size of 165 cm height, 12 cm width and 11 cm thickness. We placed SLG along the return yoke of the magnet like a hodoscope behind BDC.

Čerenkov photons from an EM shower were transported vertically by the total reflection to the photomultipliers at the top and bottom ends. we used R1911 of Hamamatsu Photonics with a diameter of 3 inches.

We tested a one-segment model. The position dependence of the light yield was obtained using a 500 MeV/c electron beam. Although the light yield at one end decreased by 75% at block by block as shown in Figures 2.30, the sum of both ends was almost flat. Typical responses for π mesons and electrons were obtained as shown in Figure 2.31. Although the effective thickness for the electron shower-development was only 7.5 radiation lengths, typical energy resolution of $15\%/\sqrt{E}$ was obtained. By keeping 95% efficiency for electrons, the π meson rejection of 2×10^{-2} can be achieved.
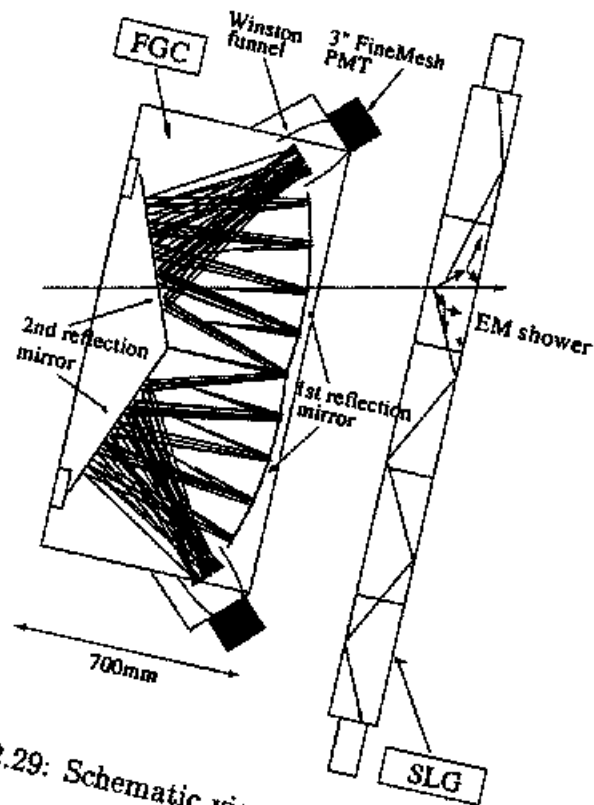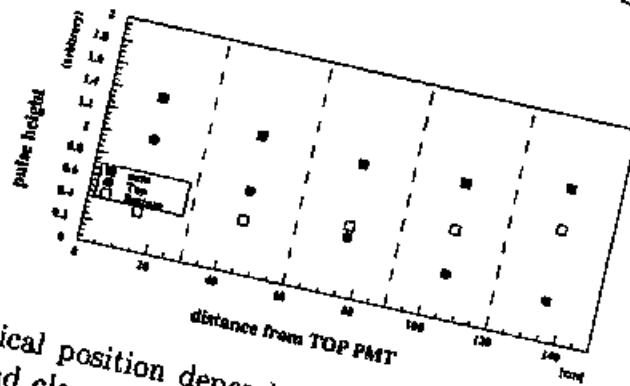
Figure 2.29: Schematic view of FGC and SLG

Figure 2.30: Vertical position dependence of the light yield for SLG. The open rectangles and closed circles are the light yield from the top and the bottom PMTs. The closed rectangles are for the sum.

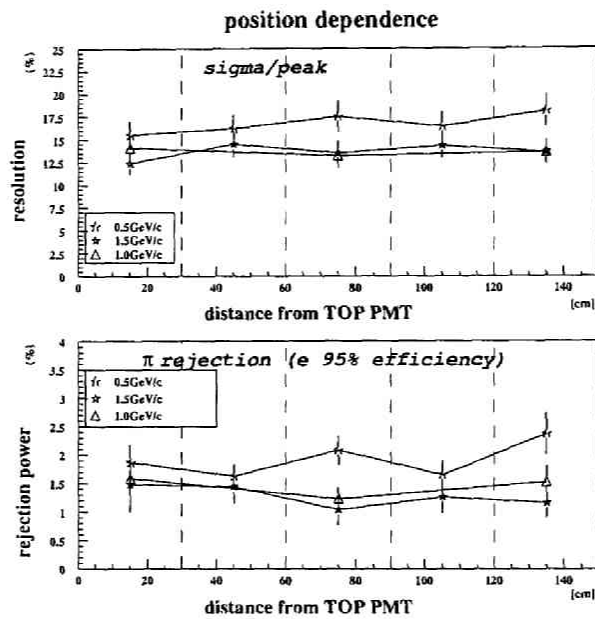Figure 2.31: The vertical position dependence of the energy resolution (top) and the π meson rejection power (bottom) of SLG. The open stars, open triangles, and closed stars correspond to momentum of 0.5 GeV/c, 1.0 GeV/c, and 1.5 GeV/c, respectively.

2.7 Trigger

The schematic diagram of the trigger control system is shown in Figure 2.32. We applied the three-level trigger logic for e^+e^- events and the two-level to obtain K^+K^- events. The both modes worked simultaneously. Hits signals from the counters and the chambers were sent to the trigger logic. If the condition of the electron or the kaon first-level trigger logic was satisfied, the event latch was set as "busy" and the gates for ADC were opened and the common start (or stop) timing signals for TDC were generated. The higher-level trigger logic was invoked at the same time. The "busy" state of the event latch was kept until the clear signal was generated by the higher-level triggers.

If the latched events satisfied all the levels of the electron or kaon trigger requirements, the event accept signal was issued and the data in the ADC and the TDC modules were transfered to the memory modules. When the data transfer was completed, the event latch was cleared and the trigger logic became ready for the next events. If the latched event did not satisfy the higher-level trigger logic, the clear signal was sent to the ADCs and TDCs and the event latch was also cleared. Typically the duration of the "busy" state was 600 μsec for the recorded events and 50 μsec for the cleared events.

In order to estimate the trigger efficiencies and to monitor the trigger logic operation, we recorded the sampled events which satisfied the lower-level trigger logics regardless of the result of the higher-level triggers. Such sampled events were about 5% of all the recorded events.

The electron trigger worked as follows. In the first level, we selected electron-pair candidates using the coincidence signal of the front-stage (FGC) and the rear-stage detectors (SLG, RLG, RGC), by requiring the horizontal position matching as shown in Table 2.6, 2.7 and 2.8. The hit signals of each segment were defined as a ORed signal of the top and the bottom PMTs. The size of the matching windows corresponds to the momentum range greater than 400 MeV To suppress electron pairs with a small opening angle, such as from Dalitz decays and γ conversions, we required the two FGC hits to be more than 2 segmentations apart. The typical trigger rate of the electron first-level was 640 per spill.

In the second level, we required the pair to be oppositely charged by using the drift chamber hits associated with the FGC hits. The hit positions in the chambers were obtained from the OR-ed signal of the X and X' layers in the outer-most layers in CDC and in BDC. The OR-ed signals provided an
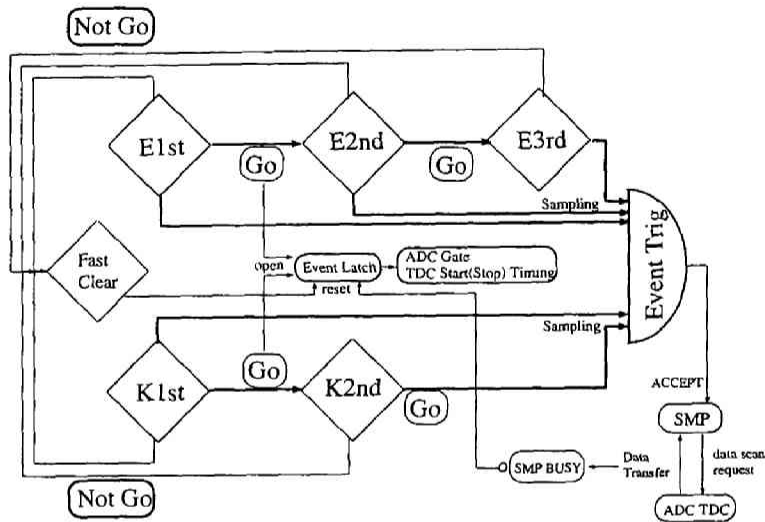
Figure 2.32: A diagram of the Trigger control system

		FGC												
		1	2	3	4	5	6	7	8	9	10	11	12	13
	1		◯											
	2		◯	◯										
R	3		◯	◯	◯									
G	4			◯	◯	◯								
C	5				◯	◯	◯							
	6					◯	◯	◯						
	7						◯	◯	◯					

Table 2.6: The pattern of the matrix coincidence for the FGC segments and the RGC segments in the electron first-level logic

		FGC												
		1	2	3	4	5	6	7	8	9	10	11	12	13
	1		O											
	2		O	O										
	3		O	O										
	4		O	O	O									
R	5		O	O	O									
L	6		O	O	O	O								
G	7			O	O	O	O							
	8				O	O	O							
	9				O	O	O	O						
	10					O	O	O						
	11					O	O	O	O					
	12						O	O	O					

Table 2.7: The pattern of the matrix coincidence for the FGC segments and the RLG segments in the electron first-level logic

		FGC												
		1	2	3	4	5	6	7	8	9	10	11	12	13
	1						O	O	O	O	O			
	2							O	O	O	O	O		
	3							O	O	O	O	O		
S	4								O	O	O	O	O	
L	5									O	O	O	O	
G	6									O	O	O	O	O
	7										O	O	O	O
	8											O	O	O
	9											O	O	O

Table 2.8: The pattern of the matrix coincidence for the FGC segments and the SLG segments in the electron first-level logic

effective angular segmentation of 1.5 degrees both at r=825 mm (CDC) and r=1605 mm (BDC). The sign of a track can be roughly determined with these segmentations together with the target position. We determined the "sign" of the track with position difference between CDC and BDC hits. We had three kinds of "sign" of the track, high momentum, positive and negative. The high momentum track had less than 6 degrees of the position difference between CDC hit and BDC hit, the positive and negative track had more than 6 degrees and less than 15 degrees. We eliminated the electron pair candidates which has an apparent "++" or "−−" configuration. We also required the remained pairs to be more than 12 degrees apart at the r=825 mm position to suppress electron pairs with a small opening angle. This logic was implemented with the hand-made modules using Field Programmable Gate Arrays (FPGA, Lattice ispLSi 3256). The typical trigger rates of the electron second-level was 550 per spill.

In the third level, approximate opening angles of the pairs were calculated. The radius of the BDC layers was almost twice larger than the radius of the outer-most CDC layers, so that the opening angle of the pair at the target, Θ_{open}, could be approximated by $\Theta_{open} = 2 \times \Theta_{cdc} - \Theta_{bdc}$, where Θ_{cdc} was the opening angle of the pair at the outer-most CDC layer and Θ_{bdc} at the BDC layer with respect to the target position. We required the Θ_{open} to be in the range from 50 degrees to 150 degrees in the trigger. This logic was implemented with the hand-made FPGA modules as the second trigger module. The typical trigger rates of the electron third-level was 430 per spill.

2.8 Data Acquisition System

The online data-acquisition system consisted of a SUN SPARC station-2 (SS-2) as a host computer together with VME or TKO based front-end electronics [32, 33]. A diagram of the data acquisition system is shown in Figure 2.33.

The Hewlett-Packard Model 743 (HP-743), VME on-board workstation, played a main role in the front-end data-acquisition system. There were thirteen Super Memory Partner (SMP) modules and a Kinetic K2917 VME-CAMAC interface-board in the VME crate. There were also thirteen TKO crates, two of them contain high resolution TDCs, three of them ADCs, and eight of them TDCs for drift chambers. The SMPs work as an interface module between the VME bus and the TKO bus via the Super Controller Head (SCH) module which was installed in each TKO crate.

Once the trigger signal was supplied to the ACCEPT input in the front panel of SMP, data scan for all the channels of ADC's and TDC's in the TKO box was performed by SCH, and the scanned data were stored in the local memories in SMP's. A busy signal was issued by SMPs during the scanning of the data, and further triggers were prohibited by the trigger control system. The process was repeated during the spill on, and at the spill end, these stored data were read out by HP-743 and written in the digital audio tape (DAT).

The scaler data were read out at the end of each spill via the VME-CAMAC interface boards connected to the Kinetic K3922 CAMAC crate controller.

The software developed for this system was based on NOVA [34]. Several processes, *collector*, *recorder* and *sender*, were running on the HP-743 with HPRT-OS and *analyzer* and *GHQ* were on the SS-2 with SUN-OS. The *collector* read the accumulated data on the memories of SMP's, and constructed the event data format. The *recorder* wrote the data to an 4 mm DAT (DDS2) via the SCSI port of HP-743, and *sender* transfered the data through Ethernet using the TCP/IP protocol to SS-2, where the data were monitored by *analyzer*. These processes were controlled and monitored by *GHQ* on SS-2.

The typical data taking rate was 2M bytes per spill which is 2 sec long, corresponding to about 800 events per spill (370 for kaon trigger and 430 for electron trigger), and the live time of the data acquisition system was about 60 %.
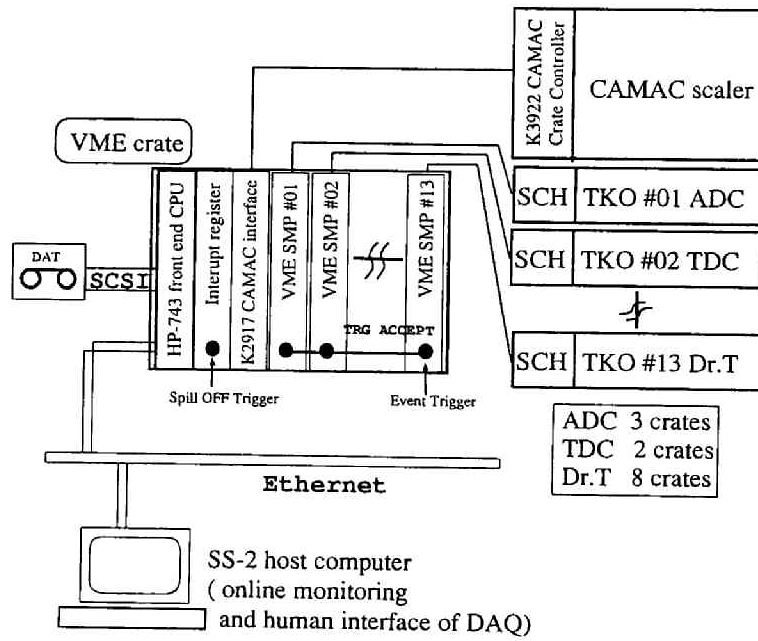
Figure 2.33: The schematic view of Data Acquisition System

Chapter 3

Analysis

3.1 Outline of the data analysis

The data described in this paper were taken in May 1998 for 22 days of the beam time. In this period, we recorded 56M events of the electron-triggered event on tapes. The used beam protons on target were 2.1×10^{14} over 131k spills, so the average proton intensity was 1.6×10^9 per spill.

First of all, the calibration of the chambers, i.e. the iterative determination of the x-t relation, as well as the position alignment of the tracking chambers were performed as described in Section 3.2. Then tracks were searched in CDC and their associated hits were examined in BDC as described in Section 3.3.1. At this stage track fitting was limited in CDC and was approximated by a quadratic function in the horizontal plane and a straight line in the vertical plane. As the first step of the event reduction, we required the events to have at least two reconstructed tracks. About 12M events (22% of the total electron-trigger events) survived after this step.

The results of the fitting in CDC gave the vertical angle of the track and the momentum in the x-y plane. Using these parameters, the track was traced to the location of the electron counters to find an associated hit. As the second step of the event reduction, we required at least one positive and one negative charged tracks. These tracks were required to have position-matched hits in both of the first and the second stage electron-counters. About 1.0M events survived after this reduction.

We refined the track fitting with the Runge-Kutta method over the magnetic-field map using both the CDC and BDC hit information, to determine the

precise momenta and the trajectories of the charged particles. In this process we re-examined the left-right assignments of the hits which were close to the wires. Using these refined trajectories, the track association to the hits in the electron counters were again examined. We required a pulse hight equivalent to 1 photo-electron in the associated FGC and RGC, and more than 0.3 GeV of energy deposit in the EM calorimeter as an electron candidate at this stage.

As the third step of the event reduction, an existence of a pair of e^+ and e^- candidates in an event was required. The number of events which passed this step was 24K. The vertex position for each events was evaluated as described in Section 3.3.4.

Before obtaining the invariant mass distribution of the electron pairs, retracking was performed for the final event samples with the constraint to require the pair to be originated from the same point on one of the target disks. We selected the events when the electron and the positron are detected in the different arms.

3.2   Calibration

3.2.1   Time offset calibration of tracking chambers

We determined relative time offsets of all the CDC and the BDC signals using the drift time spectra. The time spectrum of each wire had an edge structure close to the wire as shown Figure 3.1a. The peak position of the differentiated time spectrum (Figure 3.1b) provided the relative time offset in each signal.

This calibration was done run by run to cope with the possible temperature-dependent of the TDC system. The run dependence of the time offset was shown in Figure 3.2.

3.2.2   Determination of drift length from drift time

To convert the measured drift time to the hit position in the cell, the relation of drift length (X) and drift time (T) was determined by the procedure described below. The initial parameterization of this relation was obtained with the drift chamber simulation code Garfield. We interactively adjusted the common time-zero offset and the scaling factors of drift velocity, by min-
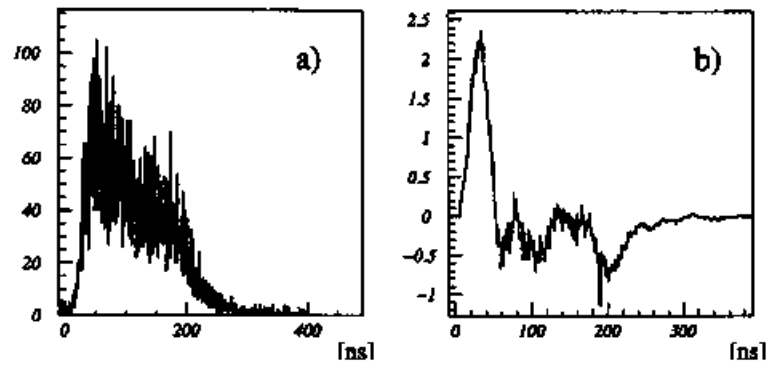
Figure 3.1: Typical TDC spectrum of CDC outer-most layer (right) and its differential (left). We determined the time offset as the peak position of the differential spectrum.
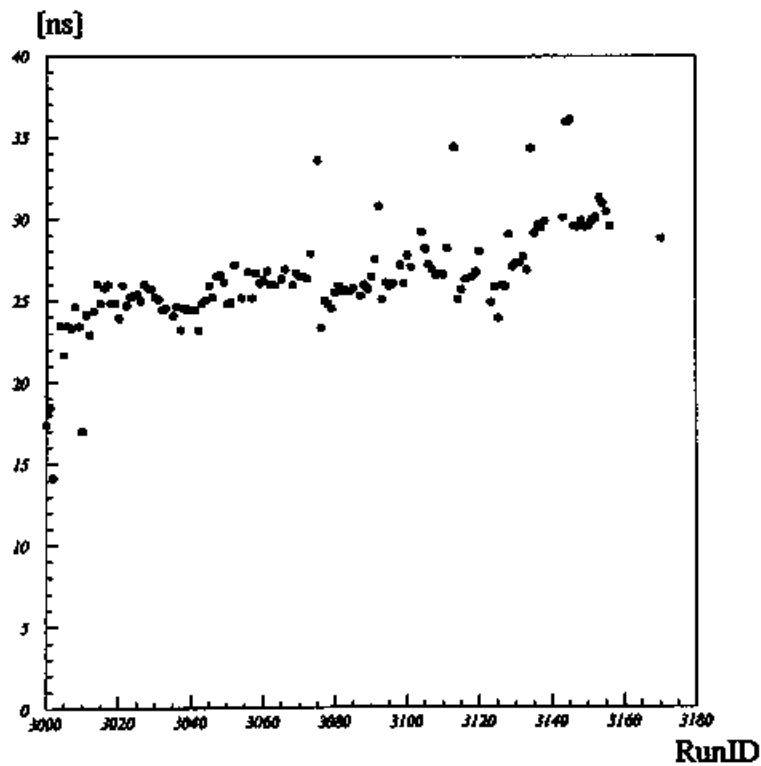

Figure 3.2: Run dependence of the time offset of typical channel in CDC.

imizing the correlation among the residuals, drift length and incident angle of the track. The residuals were calculated from the tracks obtained by the Runge-Kutta fitting as described in Section 3.3.2. We obtained the position resolution of 350 μm typically as shown in Figure 3.3.
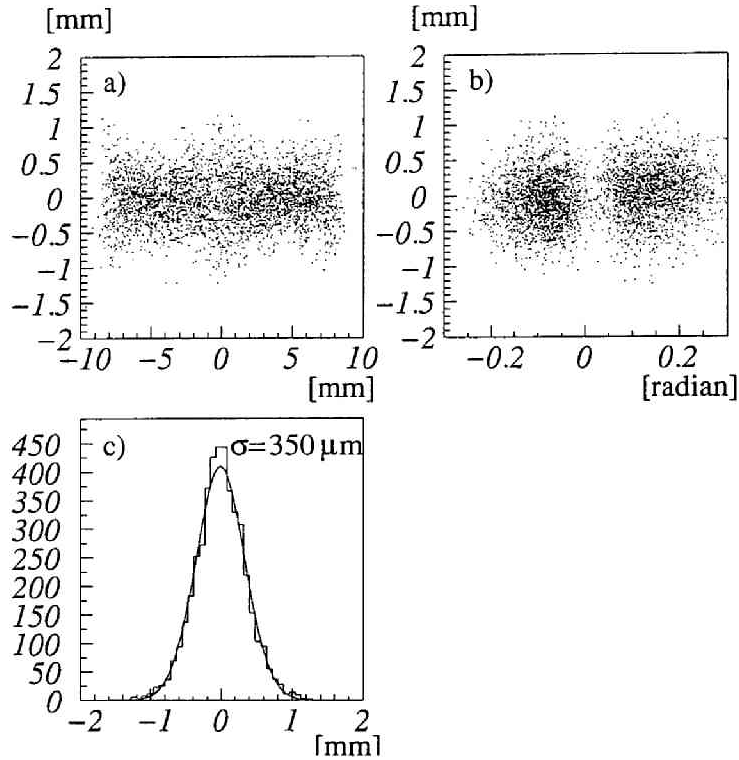
Figure 3.3: The correlations between the CDC residual as a function of the drift length (a) and of the incident angle of tracks (b). (c) shows the over all resolution.

3.2.3 Global position alignment

In the present analysis, the origin of the coordinate was set at the center of CDC. All the other chambers and counters were aligned to the CDC coordinate. The magnet position with respect to CDC was obtained by the survey done before and after the beam time. The alignment of the BDC global position with respect to CDC was also surveyed and refined using the data

taken without the magnetic field. Since the trajectories of all the particles were straight, a linear equation was adopted as a track-fitting function.

In the alignment procedure, the BDC hit position were compared with the straight track obtained with the CDC hits. Hit associations to the tracks were required in all the layer of CDC and BDC. The active area of BDC was divided into three regions horizontally. The residual distribution of the BDC hits to the CDC tracks in each region is shown in Figure 3.4. The major alignment parameters were the rotation and the relative position of BDC with respect to CDC in the x-y plane. The vertical position of BDC was taken from the survey. We have adjusted the center of the residual distribution consistently within 200 μm as shown in Figure 3.5.
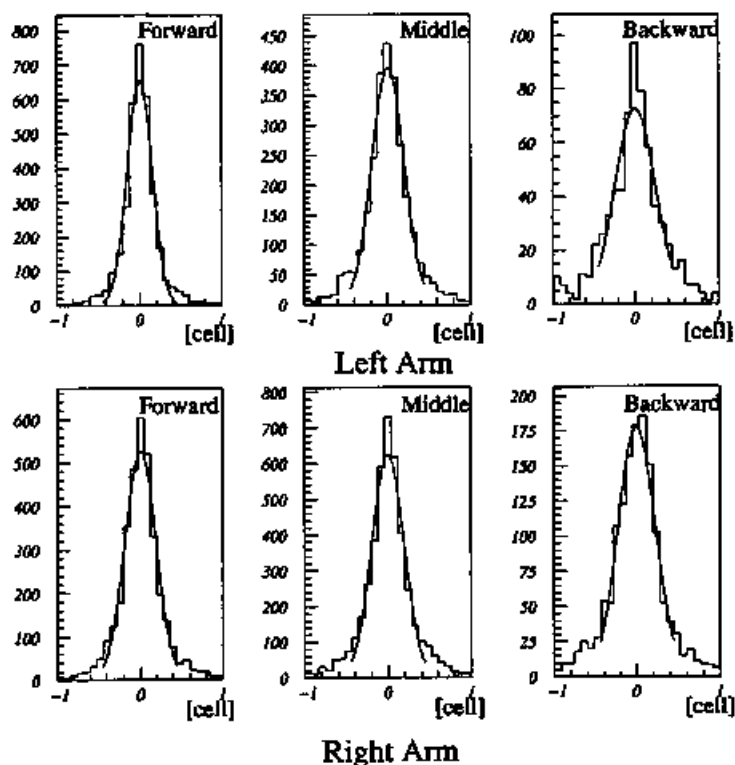
Left Arm

Right Arm

Figure 3.4: The residual distributions of the CDC extrapolated tracks at BDC in the three horizontal angular regions. The left arm results (upper figures) and the right arm results (lower figures) are shown. The unit of the horizontal axis is the cell width of BDC. The cell width is 20.81 mm.
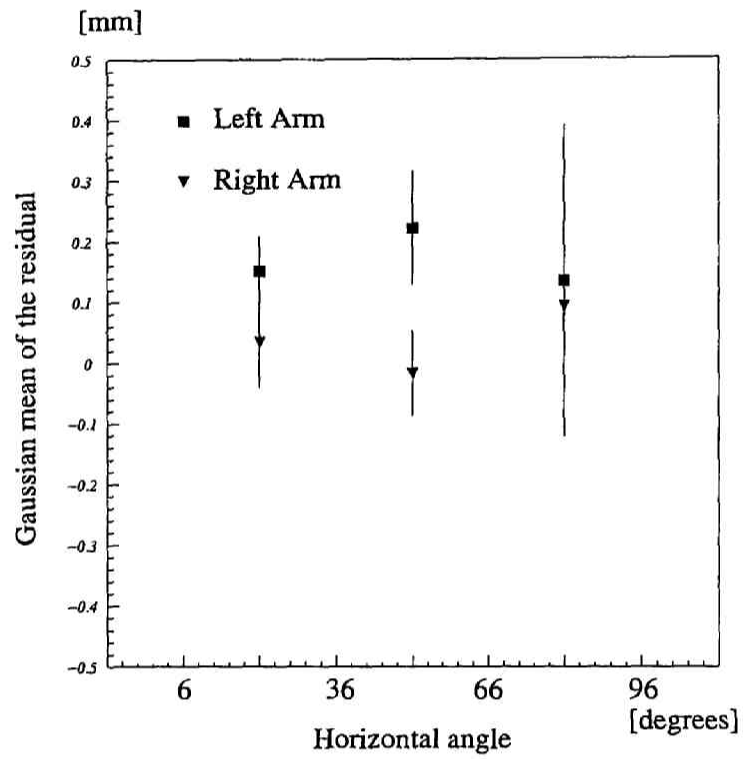
Figure 3.5: The result of BDC position alignment. The closed rectangles show the result in the left arm and the closed triangles show the right arm. The error bars are the standard deviation of the residual distributions.

3.3 Event reconstruction

3.3.1 Track reconstruction

As described in Chapter 2, CDC had ten layers of drift cells which were grouped into three super-layers. Track candidates were firstly searched using the X and X' layers in each super-layer. Since we cannot determine whether the drift direction is left or right without track fitting, each hit was treated as two independent hits in the both sides of the sense wire. To reduce CPU time for the track finding, a hit combination in the X and X' layers was regarded as a hit pair with the position at the center of the two hits. To make a pair, the hit-position difference was required to be within the momentum cut-off of 0.3 GeV/c. A hit without an associated hit in the adjacent layer was also kept as a hit candidate.

The track finding started from the most-inner X-X' pair. When a hit or a pair was found, the search windows in the middle and outer X-X' pair were set for the region corresponding to the momentum larger than 0.3 GeV/c. All the possible combinations of three hit candidates over the three super layers in the windows were picked up as the track candidates.

Since the magnetic field was almost constant at the location of CDC, a trajectory of a charged particle was approximately an circle in the x-y plane and a straight line in the r-z plane. A circle which passes over the three hit combination was drawn and required to cross the target region within distance of 50 mm from either of the three targets. We also required the vector determined locally by the hit pair should be consistent with the line tangent of the circle within 0.4 radians.

The track candidates were fitted in the x-y plane with a quadratic function. We required the reduced χ^2 of this fitting to be less than 4.5 and the residual in each hit layer was smaller than 4σ to keep the candidates for the next step.

Next, associated hits in the tilt layers were searched for each track candidate. Since there was a pair of the V-V' layers in the middle super-layer, hit pairs were made similarly to the X-X' layers. The search region of hit points in the tilt layer was limited within the neighboring five cells which was defined by the tilt angle of 0.11 radian.

Five hits out of six in the X-X' layers and three hits out of four in the tilt layers were required to be a track candidate. Additionally a candidate with seven hits was allowed when the distribution of the assigned hit was two in

the inner super-layer, three in the middle super-layer and two in the outer super-layer with three hits in the tilt layers. Now the track candidates were fit three dimensionally with a quadratic function in the horizontal plane and a straight line in the vertical plane and kept as the candidates as far as the residuals of all the hits were within 3 σ.

Track candidates in BDC were searched independently. Three hits out of four in the BDC layers (X, X', U, V) were required to form a track segment in BDC. The combination of X and X' was only made if they were apart less than one cell. And associated U and V hits were required to be in the neighboring nine cells from the hit position of the X-X' pair, which was determined by the tilt angle of 0.11 radian. If the track candidate had hits in the both tilt layers, the height difference between the U and V hits were required to be less than 30 mm at the projected positions on to the plane determined by the X-X' pair.

Then the CDC track was extrapolated to BDC, where the horizontal position matching of ± 1.2 BDC cells, the angle matching of ± 0.2 radian and the height (z) matching of 100 mm were required a final track candidate. Also the track candidates in BDC were fit with a linear function with the constraint of the vertical angle given by the CDC track, and we required the residual of each hit of BDC did not exceed 0.2 BDC cells.

When more than one BDC-track candidate were connected to one CDC track candidate, we selected CDC-BDC tracks as follows. If the BDC-track was associated with 4 hits, we kept all the BDC-track candidates and the selection was done by the Runge Kutta fitting. If the BDC-track had only 3 hits, we selected the best one as follows. First we discarded the candidate which was a subset of the other BDC-track. We selected a BDC track with the best χ^2 of the fitting with the angle fixed by the CDC-track extrapolation.

3.3.2 Track fitting by Runge-Kutta method

All the track candidates obtained in CDC with a connection to the BDC track segment were fit with the Runge-Kutta method to determine the refined momentum and the precise trajectory. The particle trajectories were traced in a 50 mm step through the magnetic field map calculated with TOSCA.

The Runge-Kutta track tracing started from the surface of a virtual cylinder with a diameter of 100 mm located at the center of the magnet. The initial starting point and the initial momentum vector for the minimization were given by the track candidate obtained in CDC.

In each trace by the Runge-Kutta method, a reduced χ^2 was calculated along all the hit positions. The χ^2 value was minimized with a help of the minimization code MINUIT [35]. The distribution of the calculated reduced χ^2 of the final sample is plotted in Figure 3.6. This distribution is consistent with χ^2-distribution. In the calculation of the reduced χ^2 we took into account the resolution of each layer of the drift chambers obtained as residual, described in Section 3.2.2.
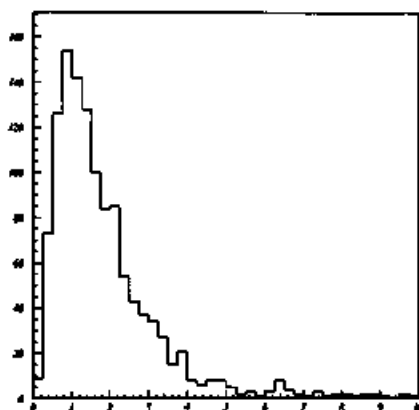

Figure 3.6: Reduced χ^2 distribution in the Runge-Kutta fitting.

Finally, if there are two or more CDC track candidates sharing more than two common hit in CDC or BDC, we selected the track candidate with the best χ^2 in the Runge-Kutta fitting and discarded others.

3.3.3 Evaluation of momentum reconstruction

To evaluate the performance of the spectrometer, the mass resolution was examined for the observed peaks of $\Lambda \rightarrow p + \pi^-$ and $K_s \rightarrow \pi^+ + \pi^-$ decays as shown in Figure 3.7 and 3.8. For the Λ peak we obtained the centroid at 1115.5 MeV/c^2± 0.03 (known to be 1115.7 MeV/c^2) with the Gaussian resolution of 1.8 ± 0.1 MeV/c^2, and for K_s 493.9 MeV/c^2± 0.1 (known to be 497.7 MeV/c^2) and 3.6 ± 0.6 MeV/c^2, respectively. The observed peak positions and the widths give the systematic uncertainty of the mass scale and the mass resolution of the present analysis. The possible origin of the mass scale uncertainty for the K_s is the momentum scale uncertainties and opening angle measurement uncertainty. For the K_s case the contribution of
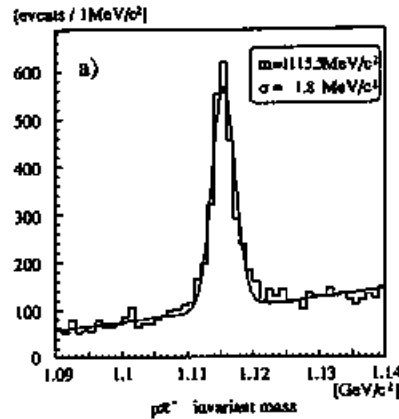
Figure 3.7: Invariant mass spectrum of p π^- The curve was the best fit result with the Gaussian with a linear background. The vertex position were required to be more than 20 mm apart from the target.
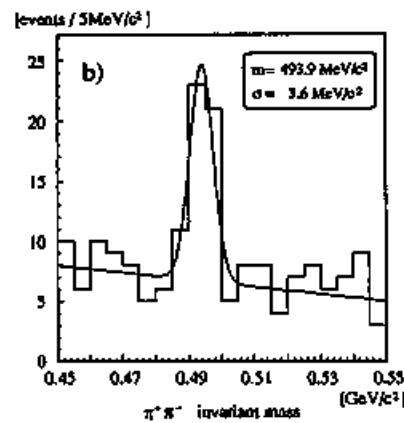

Figure 3.8: Invariant mass spectrum of $\pi^+\pi^-$ The curve was obtained as the best fit result applying the Gaussian with a linear background. The vertex position were required to be more than 10 mm apart from the target.

the momentum scale uncertainty is large, also there is same situation for the ω and ϕ mesons case. The mass scale uncertainty for the ω and ϕ mesons was estimated from the K_s case to be 4 MeV/c^2 and 7 MeV/c^2, respectively.

The results were compared to the Monte Carlo simulations in which we took the chamber resolution and the multiple scattering into account. The observed widths were well reproduced by the simulation (1.9 MeV/c^2 for Λ and 3.5 MeV/c^2 for K_s), and The mass resolution for the ω and ϕ mesons was estimated to be 9.6 MeV/c^2 and 12.0 MeV/c^2, respectively.

3.3.4 Vertex reconstruction

The vertex point of the interaction was determined as follows. All the tracks in each events were traced back with the Runge-Kutta method to the target region, where we obtained the cross points of these tracks on the plane y=-4.2 mm which corresponded to the center of the beam position in the y-axis. The x-coordinates and the z-coordinates of the cross points were averaged to give the initial point for the vertex finding.

Next, we defined a reduced χ^2 (χ_R^2) of the vertex fitting as

$$\chi_R^2 = (\sum_{j=1}^{N_t}[(d_x^j/\sigma_x)^2 + (d_y^j/\sigma_y)^2 + (d_z^j/\sigma_z)^2])/(3N_t - 4)$$

where N_t is the number of the tracks, d_j^i(i=x,y,z) is the distance between a vertex point to be searched and the nearest point of the j-th track in each axis, and the weighting factor σ_i represents the error of the track-vertex determination in each axis. The factors σ_i(i=x,y,z) were determined as σ_x = 1.1 mm, σ_y = 1.8 mm, and σ_z = 7.2 mm. We searched for the point where we got the minimum χ_R^2 with MINUIT. When the fitting process was converged, the point was determined as the vertex. We examined the quality of the determined vertex by requiring the equation below to be satisfied for each track-j.

$$[(d_x^j/3\sigma_x)^2 + (d_y^j/3\sigma_y)^2 + (d_z^j/3\sigma_z)^2] < 1.0$$

We discarded the tracks which did not satisfy this requirement, and re-determined the vertex from the remaining tracks with the same fitting procedure. The reconstructed vertex distribution is shown in Figure 3.9. The three targets were clearly seen. The vertex resolution was estimated to be 5 mm.

The vertex position were required within 10 mm in the horizontal axis (y) and within 20 mm in the beam direction axis (x) from one of three targets. We also required the χ^2_R to be less than three in the final event sample.
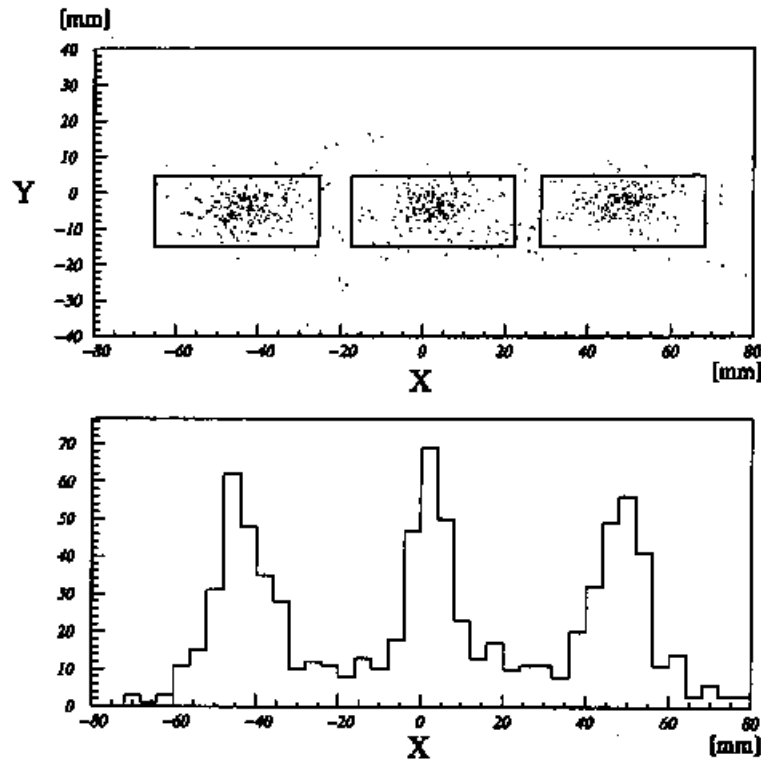
Figure 3.9: Vertex distribution in the xy-plane (upper) and the projection in the x-axis (lower). The indicated rectangles in the upper figure are the cut regions for the vertex position in the x-y plane.

For the final e^+e^- pair tracks we repeated the Runge-Kutta fit procedure by requiring that the pair tracks were originated from the same point on the target disk determined as described above.

3.3.5 Electron Identification

Electron Identification with Gas Čerenkov counters

The horizontal position matching of FGC to the Runge-Kutta tracks is shown in Figure 3.10. We defined a matching window to be within ±1 counter size. The hit in FGC was defined when the ADC sum from the top and the bottom photomultipliers of the segment exceeded 200 channel, which corresponds to about 1 photo-electron. The FGC ADC spectrum for the final electron-pair sample is shown in Figure 3.11 and the discriminator TDC signal had a good timing as shown in Figure 3.12. The figure shows the distribution of the hit-timing difference between FGC and the start-timing which was determined by STC. We required the difference to be less than 10ns.

The correlations between the dip angle of the Runge-Kutta tracks and the asymmetries of the ADC sums for the top and bottom photomultipliers are shown in Figure 3.13 for the electron candidates. The asymmetry A was defined as

$$A = \frac{\sum A^{top} - \sum A^{bottom}}{\sum A^{top} + \sum A^{bottom}}$$

where $A^{top}(A^{bottom})$ is the ADC counts of the top (bottom) photomultiplier and the summation was made over the phototubes which satisfied the position matching criteria. Since the Čerenkov angle for $\beta=1$ particles were 0.06 radian, the tracks whose dip angle was within ±0.06 radians could produce hits both in the top and the bottom photomultipliers. The regions shown in the Figure 3.13 are used for the electron selection.

For RGC, the horizontal position matching to the Runge-Kutta tracks was required as same as FGC. The RGC hit was defined when the ADC sum from the top and the bottom photomultipliers of the segment exceeded 50 channel, which corresponds to about 1 photo-electron. The same timing requirement as for FGC was adopted. Since the vertical acceptance of RGC is ±0.1 radian, we required the dip angle of the track to be less than 0.12 radian.

Electron Identification with Lead Glass calorimeters

The horizontal position matching of RLG to the Runge-Kutta tracks is shown in Figure 3.14. We defined a matching window to be within ±1 counter size. The hit association with RLG or SLG was defined when the sum of the energy-loss from the horizontally-associated three segments exceeded 0.3
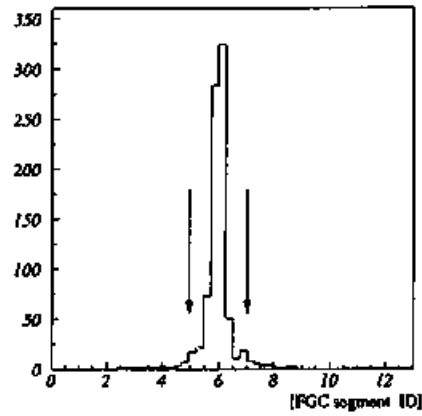
Figure 3.10: Horizontal matching between electron track and FGC hit. Electron tracks are selected as described in 3.3.6. The arrows indicates the region for the electron selection.
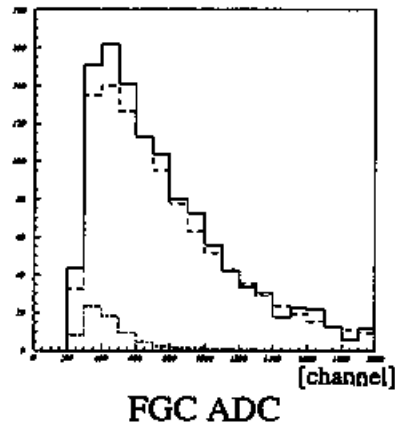

FGC ADC

Figure 3.11: The FGC ADC spectra for the final electron-pair sample. The solid line corresponds to the final electron candidates, the dashed line corresponds to the pure electron and the dot-dashed line corresponds to the π meson. The relative abundance of the electron and the π meson were obtained through the fit as described in Section 3.3.6.
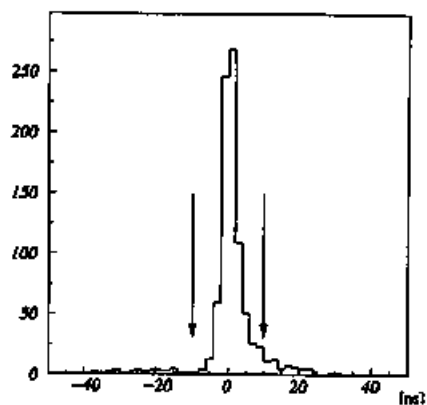
Figure 3.12: TDC spectrum of FGC hits. The arrows indicates the region of the good timing.
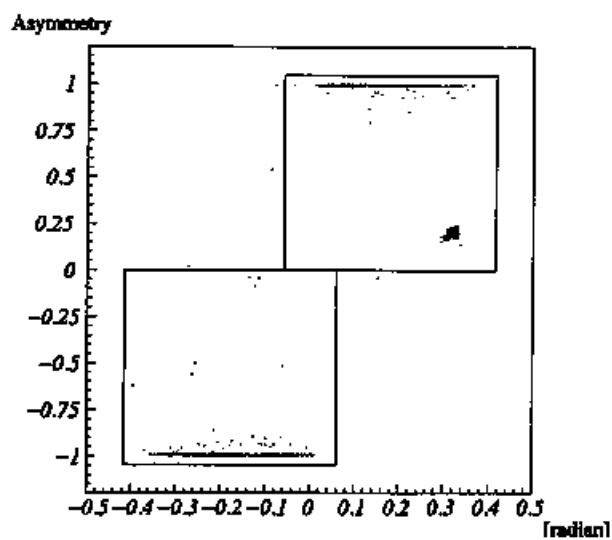
Figure 3.13: The correlation between the FGC ADC asymmetry and the track dip angle. The tracks outside the boxes were eliminated from the electron candidates.

GeV and the energy loss over the momentum (E/p) was more than 0.3 and less than 3.0 as shown Figure 3.15. Since the vertical acceptance of RLG is from ±270 mm to ±880 mm from the beam line, we required the vertical position of the track at RLG to be from ±260 mm to ±890 mm.
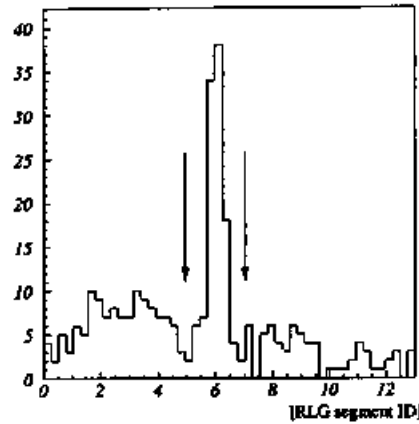
Figure 3.14: Horizontal matching between electron track and RLG hit. Electron tracks are selected as described in 3.3.6.

3.3.6 Efficiency of Electron Identification

To evaluate the efficiency of electron identification, we collected pure electron sample from the data using the conversion and Dalitz pair electrons. When we calculated the invariant mass at the very low mass part, they appeared as a clear peak at m_{ee}=0 as shown in Figure 3.16. We defined the mass region below 0.025 GeV/c^2 as an electron pair from the gamma conversion or the Dalitz decay. To avoid the trigger-bias, we selected the events which have three tracks including such a low-mass pair. Since the conversion or Dalitz decay electron pair did not satisfy the opening angle condition of the third-level trigger, the event should be triggered by the third track and one from the electron pair. As a no-bias electron, we selected one of the electron pair tracks which had the same charge as the third track. Using these no-bias electrons the detection efficiencies were obtained as described below.

To suppress the fake triggers caused by π mesons and protons, we set the discriminater threshold for the gas Čerenkov counters higher than the optimum setting for electrons, thus the electron efficiency was sacrificed. For
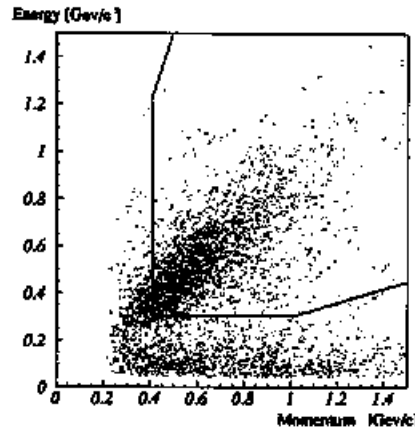
Figure 3.15: The correlation between RLG energy and momentum. The region is used for the electron selection.

electrons with a momentum greater than 400 MeV/c, the overall efficiencies including the trigger threshold and the off-line cut were 55% for FGC, 86% for RGC and 85% for the calorimeters, RLG and SLG. The electron efficiency as a function of the threshold of the momentum cut is shown in Figure 3.17. We selected the electron with a momentum greater than 400 MeV/c.

Next, we evaluated the π meson rejection factor. We made the pure π meson sample by requiring the veto of the second-stage electron counters. From the ADC spectra for this sample, we calculated the π meson rejection factor for each detector and multiplied the result from FGC by the result from second stage detectors. We achieved the π meson rejection of 6.7×10^{-4} with a cascade operation of FGC and the EM calorimeters, and 3.9×10^{-4} with FGC and RGC for 400 MeV/c π mesons.

Finally, we evaluated the π meson contamination in the final electron-pair sample using the ADC histogram of FGC, as shown in Figure 3.11. The ADC spectrum for electrons and π mesons was obtained from the pure electrons and π mesons sample described before. The relative abundances of the electron and the π meson were obtained through the fit on the ADC spectrum of FGC for the final e^+e^- pair. The remaining $e^-\pi^+$ and $e^+\pi^-$ background was estimated to be $13 \pm 6.8\%$.
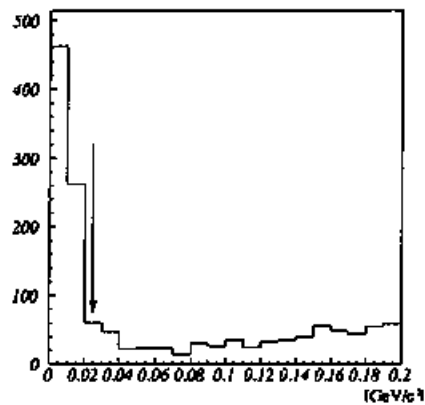
Figure 3.16: Invariant mass spectrum of electron pair in the low mass region. The region below the arrow was used for the pure electron sample.
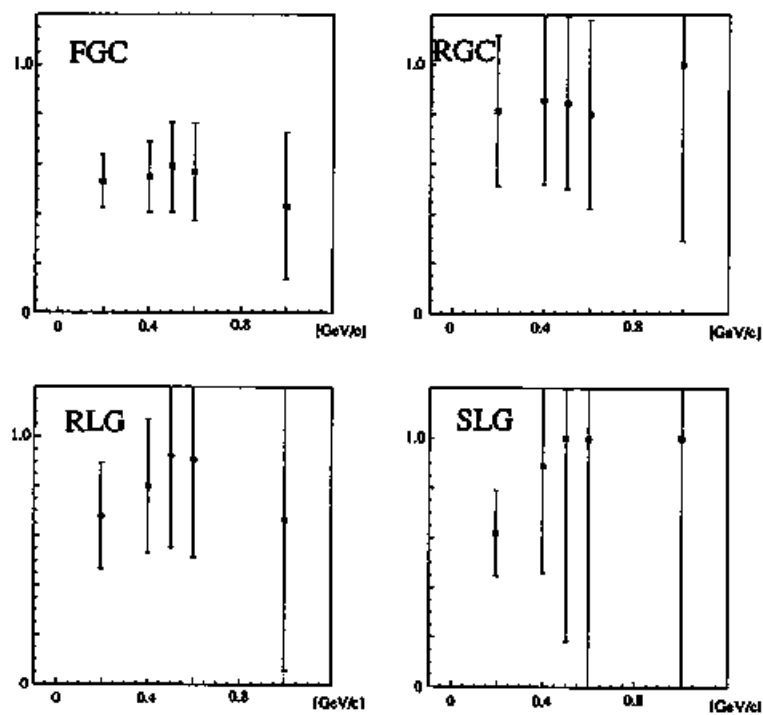

Figure 3.17: The electron detection efficiency as a function of the threshold of the momentum cut.

3.3.7 Acceptance of e^+e^- pair

The chamber acceptance cut for the target positions

Since we used the three targets simultaneously and they were placed 40 mm apart from each other, the acceptance of the spectrometer for each target is different from each other. We required additional cut to ensure the same acceptance for all the three targets. The target placed at the most downstream position had the smallest acceptance and we restricted the acceptance of the other targets as same as that of the downstream target. This cut was applied for the events which had the positive charged particle in the left arm and the negative charged particle in the right arm. The minimum horizontal angle for such an electron is 15.8 degrees with respect to the beam line.

To evaluate the influence of this cut, we applied this cut condition for the Monte Carlo data, which were generated by the nuclear cascade code JAM [36]. We obtained the distribution of the invariant mass of the uncorrelated electron pair, as shown in Figure 3.18, from the mixed events of electron-positron pairs of the π^0 Dalitz decays generated by JAM. The acceptance difference between the targets is visible in Figure 3.18. After the acceptance cut, the difference of acceptance for the each targets in the mass region above 550 MeV/c² is negligibly small, especially when we take the average of the up and downstream targets and compare with the middle target data.

The invariant mass acceptance

We evaluated the experimental mass acceptance using the mass distribution of the ρ meson obtained by JAM [36]. Since the ρ meson has the broad peak, we can evaluate the mass acceptance as the ratio of the accepted ρ mesons to the generated ρ mesons. The mass acceptance normalized at 2.0 GeV/c² is shown in Figure 3.19. We selected the events when the electron and the positron are detected in the different arms, so that the acceptance is largely suppressed at the low mass region. The overall acceptance of the spectrometer in the measured region ($0.6 < y_{ee} < 2.2$, $0.0 < P_{t\,ee} < 1.5$ GeV/c) was about 4% for ρ meson mass.
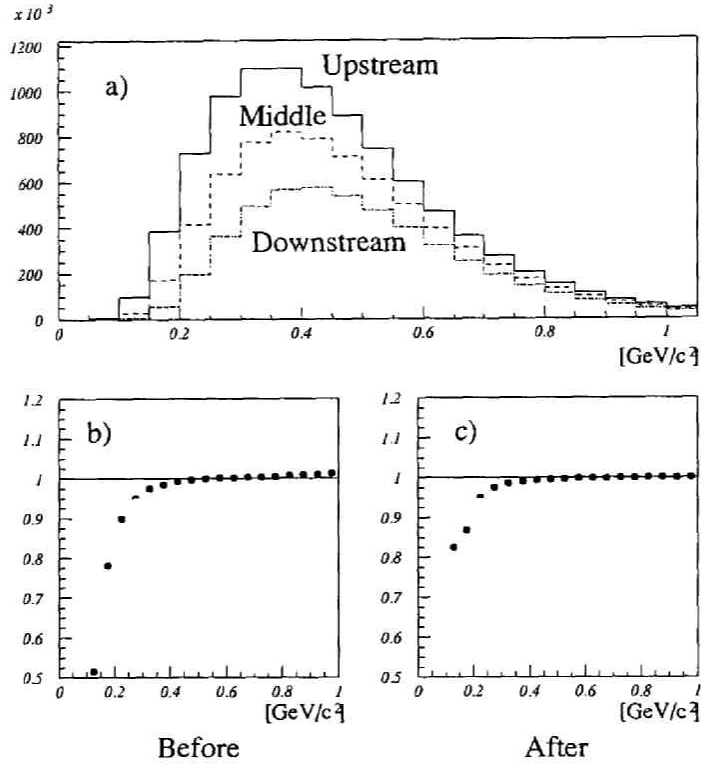
Figure 3.18: The upper figure (a) shows the mass spectra of e^+e^- obtained from the mixed event of $\pi^0 \to e^+e^-\gamma$ generated by JAM. The solid line corresponds to the upstream target(C, CH_2), the dashed line corresponds to the middle target(Cu) and the dotted line corresponds to the downstream target(C, CH_2). The lower figure (b) shows the ratio of the e^+e^- pairs as the function of its invariant mass distribution between the average of the upstream and the downstream targets and the middle target. (c) shows as same as (b) but after the acceptance cut.
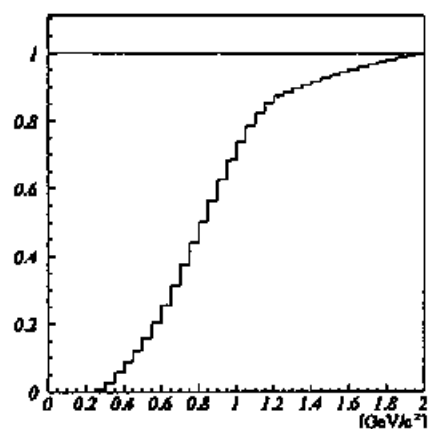
Figure 3.19: Acceptance for the ρ mesons as the function of the invariant mass of electron pair, normalized at 2 GeV/c^2.

Chapter 4

Results and Discussion

4.1 Invariant mass distribution of e^+ e^- pair and kinematical distribution

The invariant mass spectra of e^+e^- pairs are shown in Figure 4.1 for the carbon and polyethylene targets (light nuclear targets) sample and in Figure 4.2 for the copper target (heavy nuclear target) sample. The samples are for the e^+e^- pairs observed as each in the different arm, so that the low mass side of the spectra is largely suppressed. Although the clear peaks of the ω meson decaying into e^+e^- is visible in the spectra, a shape difference is observed between the light nuclear targets and the heavy nuclear target. The difference is statistically significant as will be explained in the following sections, and is characterized as an excess in the low mass side of the ω peak.

The measured opening angle, $\beta\gamma_{lab}$, transverse momentum and rapidity distributions of the electron-positron pair is shown in Figure 4.3 for the light nuclear targets and in Figure 4.4 for the heavy nuclear target. The combinatorial background was already subtracted as obtained by the event mixing method as explained in Section 4.1.1. It can be seen the kinematical coverage of the present data is $0.6 < y_{ee} < 2.2$, $0.0 < P_{t\,ee} < 1.5$ GeV/c and $1 < \beta\gamma_{ee} < 4$. There is no significant difference between the light and the heavy target.
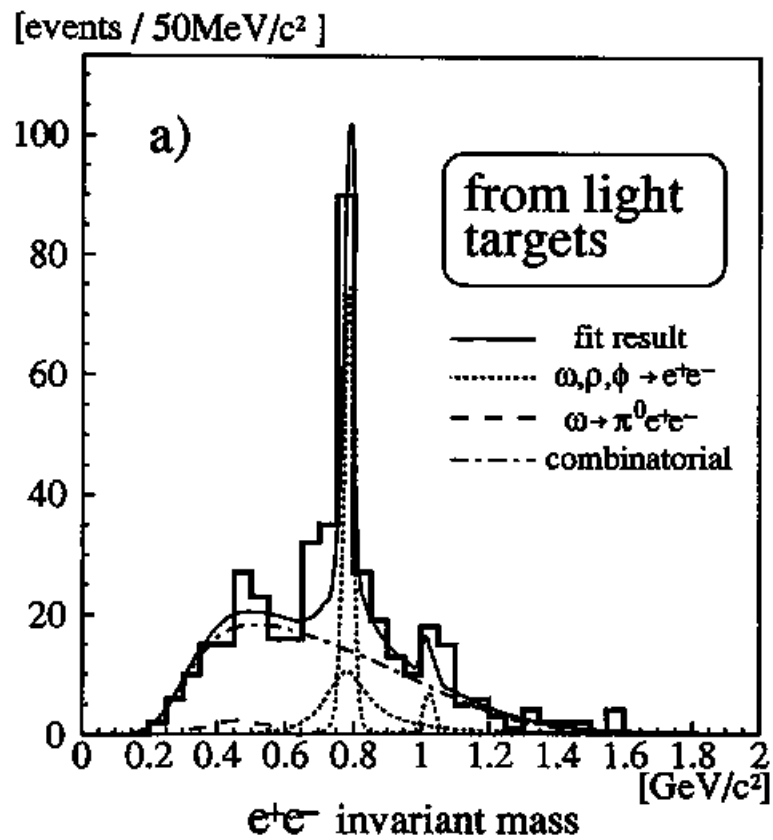
Figure 4.1: Invariant Mass spectrum for the light nuclear targets. The solid lines show the best-fit results of the known hadronic sources with the combinatorial background. The contributions of individual decay channel are also shown.
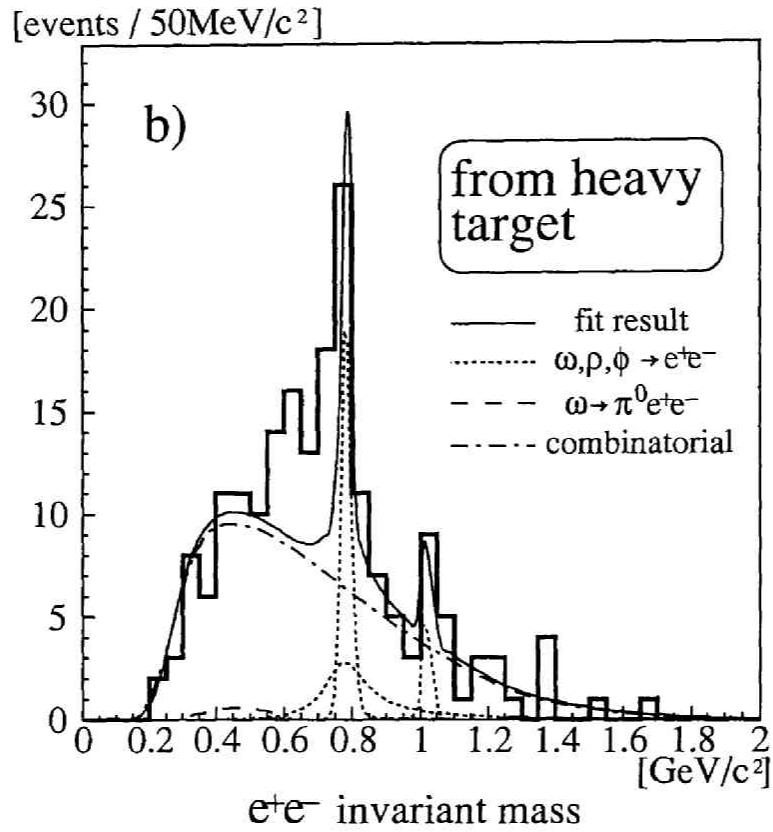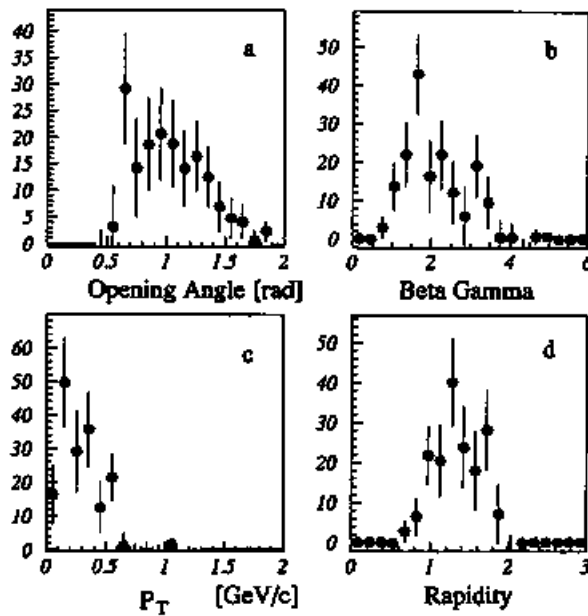
Figure 4.2: Invariant Mass spectrum for the heavy target. The solid lines show the best-fit results of the known hadronic sources with the combinatorial background. The contributions of individual decay channel are also shown.

Figure 4.3: The distributions of the opening angle (a), $\beta\gamma_{lab}$ (b), transverse momentum (c), rapidity (d) of the e^+e^- pairs from the carbon and the polyethylene targets. The combinatorial background was already subtracted in the figures.
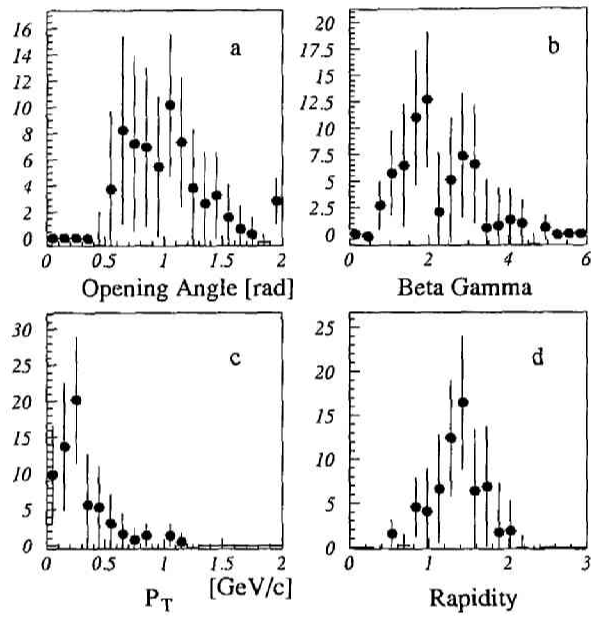
Figure 4.4: The distributions of the opening angle (a), $\beta\gamma_{lab}$ (b), transverse momentum (c), rapidity (d) of the e^+e^- pairs from the copper target. The combinatorial background was already subtracted in the figures.

4.1.1 Background estimation

We have tried to reproduce the mass shape of the obtained histograms with the combinatorial background and the known hadronic sources. The origins of the combinatorial background were the pairs which were picked up from two independent Dalitz decays or γ conversions, and the pairs like $e^-\pi^+$ or $e^+\pi^-$ due to the particle misidentification. By taking into account the π meson rejection power estimated in the section 3.3.6, the remaining $e^-\pi^+$ and $e^+\pi^-$ background was estimated to be about 13% in the spectra and the contaminations like $\pi^+\pi^-$ to be negligibly small. The distribution of the combinatorial background was obtained from the event mixing method, so that the distribution should reflect the actual combinatorial-pair contribution (e^+e^-, $e^-\pi^+$ and $e^+\pi^-$) automatically. The detail description of the combinatorial background and event mixing method is described in Appendix A. As the known hadronic sources, $\rho \to e^+e^-$, $\omega \to e^+e^-$, $\phi \to e^+e^-$, $\eta \to e^+e^-\gamma$ and $\omega \to e^+e^-\pi^0$ were considered. The Dalitz decay, $\pi^0 \to e^+e^-\gamma$, is negligible in the mass acceptance of the present data. The shapes of the e^+e^- invariant mass spectra from the Dalitz decays, $\eta \to e^+e^-\gamma$ and $\omega \to e^+e^-\pi^0$, were taken from the reference [37].

The mass shape of the ρ, ω and ϕ mesons was given as the Breit-Wigner function with the natural width of 150 MeV/c^2, 8.41 MeV/c^2 and 4.43 MeV/c^2, respectively. The Breit-Wigner functions were smeared with the estimated mass resolution of 9.6 MeV/c^2 for the ω and 12.0 MeV/c^2 for the ϕ meson.

The present experiment used the targets with radiation lengths of less than 0.3% so that the radiative tail and the multiple scattering due to the target thickness were negligible. We have assumed that the production cross section of ρ is equal to that of ω following to the data obtained in 12 GeV p+p interactions [38]. The mass acceptance for the known sources is obtained by the cascade code JAM as explained in Section 3.3.7. The relative abundances of the known sources and the combinatorial background were obtained through the fit with four parameters, the amplitudes of $\rho/\omega \to e^+e^-$, $\phi \to e^+e^-$, $\eta \to \gamma e^+e^-$ and the combinatorial background. The amplitude of the other source, $\omega \to \pi^0 e^+e^-$, was given from the branting ratio.

The best fits are over plotted in Figure 4.1 and 4.2. The contribution of $\eta \to \gamma e^+e^-$ turned out to be negligible. As the result of the fits, we found 75.5 ± 9.0 ω mesons and 7.4 ± 5.8 ϕ mesons from the light target and 20.0 ± 4.8 ω mesons and 5.2 ± 2.7 ϕ mesons from the copper target. The invariant

mass shapes were well reproduced except the mass region below the ωpeak.

4.1.2 Evaluation of excess

To evaluate the excess in the mass region from 550 MeV/c^2 to 750 MeV/c^2, we fit the histograms again by excluding this mass region. The best fit result are shown in Figure 4.5. The excess was estimated by subtracting the amplitude of the fit function from the data. The number of excess in the light nuclear target data is 19.6 ± 11.7 and that of the copper target is 29.5 ± 8.7. The excess is statistically significant for the copper target data. The ratios to the amplitude of the ωpeak are 0.26 ± 0.16 for the light target and 1.48 ± 0.56 for the heavy nuclear target. The fit results are listed in Table 4.1.
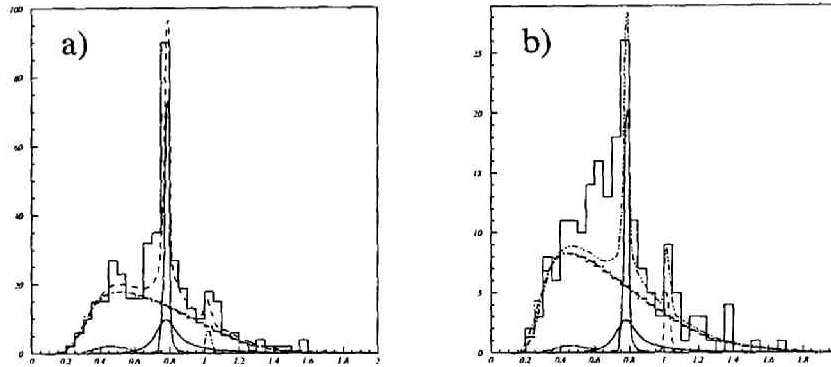
Figure 4.5: Invariant mass spectrum of the electron pairs: a) for the carbon and polyethylene targets and b) for the copper target. The cocktail curves are obtained as same as in Figure 4.1 and 4.2 except the fitting onto the histograms were performed excluding the mass region from 550 MeV/c^2 to 750 MeV/c^2

4.2 Discussion

The difference between the light and the heavy target cases should be originated from the difference of the nuclear size. The natural explanation of the shape change is that the mass modification of ρ/ω mesons takes place

	fit for all the mass region		fit excluding the excess region	
	light	heavy	light	heavy
N_ω	75.5 ± 9.0	20.0 ± 4.8	73.5 ± 9.0	20.2 ± 4.9
N_ϕ	7.4 ± 5.8	5.2 ± 2.7	7.4 ± 5.8	5.8 ± 5.6
N_{excess}		-	19.6 ± 11.7	29.5 ± 8.7
N_{excess} / N_ω		-	0.26 ± 0.16	1.48 ± 0.56

Table 4.1: The table of the number of ω, ϕ, excess and the ratio of excess over ω for each fitting and each target.

inside a nucleus. First, we discuss the width of the ρ/ω mesons in the nuclear medium, because the number of mesons decaying inside a nucleus, which determined with the width and the production position, is needed to evaluate the amount of excess. Next, we discuss the possible origin of the observed mass-shape modification, such as trivial kinematical effects and the Hatsuda-Lee prediction.

The present experiment was designed to observe the effect predicted by Hatsuda and Lee using the QCD sum rule. However the QCD sum rule has a weak point, that it can predict the amount of mass shift under the constraint of QCD but it has no capability to predict how the modified shape looks like. To understand the nature of the present results, it is thus required to consider;

1. Physics mechanisms which can cause the mass shift of the vector mesons.

2. In medium broadening of the vector mesons which causes the modified shape of the mass spectrum and at the same time determines also the in-media decay rate.

We observed slowly moving e^+e^- pair whose $\beta\gamma_{lab}$ were from 1 to 4. For the mesons with such kinematical distribution about 60% of ρ mesons and about 10% of ω mesons are to decay statistically inside a copper nucleus if there isn't any mass broadening in nuclear medium. For this estimation of the in-medium decay rates, we assumed ρ/ω are produced in the surface of a nucleus as expected from the $A^{2/3}$ dependence of the production cross section of ρ and ω meson [23]. These decay rates are obtained as the number of the ρ/ω mesons decaying where the density is greater than $1/2 \, \rho_0$ over the number of ρ/ω mesons decaying outside nucleus. The Woods-Saxon density

distribution of a nucleus and the momenta of the ρ/ω mesons given by JAM were taken into account in this estimation. If the width of ω meson become as wide as the ρ meson, say 130 MeV, we would expect that in-medium decay rate of ω mesons becomes 54% in a copper nucleus and 30% in a carbon nucleus compared to the mesons decaying outside the nuclei.

Such a broadening of the ω meson is indeed suggested by the theoretical model. F Klingl *et al.* made a calculation about the modification and the broadening of the vector meson using an effective Lagrangian which combines the chiral SU(3) dynamics using the vector meson dominance [39]. They obtained the mass shift of the ω meson being consistent with the result of Hatsuda and Lee, with significant broadening of the width as large as 130 MeV/c^2, 15 times larger than in free space. For the ρ meson, the mass decreases a few MeV/c^2, while the width increases very strongly ($\sim$400 MeV/c^2). Thus according to their prediction the ρ meson peak is shifted downwards a bit and the mass shape is broadened and modified largely, and almost all the ρ mesons decay inside a nucleus. For the ω meson, the peak is shifted downwards by 100 $\sim$ 200 MeV/c^2 and is broadened in a nucleus, and makes the second peak or the excess in the low mass side of the ω peak which corresponds to the ω's decaying in free space.

There is another theoretical work by D. Cabera *et al.* [22] on the shift and broadening of the ρ meson. They calculated the properties of the ρ meson at rest in cold symmetric nuclear matter by applying the lowest order Chiral Perturbation Theory (χPT) including explicit resonance fields. They reported the shift to be 70 MeV and the broadening to be around as 400 MeV/c^2 for the ρ meson, three times larger than in free space.

Here we would like to discuss on the relation to the observed spectra. The excess were experimentally determined as 19.6 $\pm$ 11.7 for the light nucleus (carbon and polyethylene) and 29.5 $\pm$ 8.7 for the heavy nucleus target. The excesses are caused not only by ω broadening but also by ρ, regardless of the value of mass shift, because ρ meson has larger width than ω meson.

Now we consider the origin of the mass shift. It is quite interesting that the QCD inspired theories [13, 39] predicted similar mass shift of the ω meson. We have to, however, consider trivial effects which can imitate the mass shift, before relating the present result to the QCD based theories. There have been proposed two kind of kinematical effects, threshold effect and collisional broadening.

First, we would like to mention that the threshold effect is negligible in our kinematics region. The threshold effect is the influence of the subthreshold

ρ-meson production through $pp \to N^*p$ reaction. The threshold effect is measured through the dielectron production in nucleus-nucleus reactions at a beam kinetic energy of 1.0 A GeV by the Dilepton Spectrometer (DLS) at LBNL [17]. They observed an excess in the mass region below 0.7 GeV/c^2 over the expected sources. In pp reactions, there is a theoretical work which explains the threshold effect as the influence of the decay mode of N(1520) $\to \rho p \to e^+e^-p$ [40]. According to this theory, in 12 GeV pp interactions, the contribution of ρ mesons stemming from the N(1520) is only about 1% of the total inclusive ρ-production cross section. It should be noted that experimentally such modification of ρ meson is not observed in 12 GeV pp interactions [38].

Next, there is another possibility proposed by T. Yamazaki and Y. Akaishi [41]. They calculated the modification of ρ mesons by the kinematical effects, which is called as *collisional broadening*. They take the two-body correlation between the ρ meson and a surrounding nucleon into account. They considered two decay modes, two-body-correlation decay mode ($\rho + N \to e^+e^- + N$) and normal decay mode ($\rho \to e^+e^-$). The spectral function of ρ mesons is shown in Figure 4.6. According to their calculation, the excess, caused by the two-body-correlation decay mode in the mass region from 550 MeV/c^2 to 750 MeV/c^2 is about 10% of the ρ mesons decaying normally in a nucleus. This effect is expected to cause a small influence on the mass shape, however it seems to explain the mass excess.

Finally, we compare the present results with the prediction by Hatsuda and Lee [13]. It should be noted that the excess in the copper target data is visible in the mass range about 200 MeV below the ω peak. This range is consistent with the predicted shift. To make the situation clearer we have performed a toy-model calculation to visualize how the observed spectrum should look like using the $\rho/\omega \to e^+e^-$ decays produced by JAM. The results are shown in Figure 4.7.

The assumption in the calculation is as same as the calculation shown in Figure 1.4, except for that the mass shift predicted by Hatsuda and Lee was introduced and the in-medium decay rate, i.e. the in-medium width, was varied systematically. The production cross section of ρ and ω meson were fixed at one to one, and possible ρ/ω interference was neglected. The result of the calculation is summarized in Table 4.2. It can be concluded that when we apply the broadening of the width of ρ/ω, the toy-model provides reasonable description of the present observation.

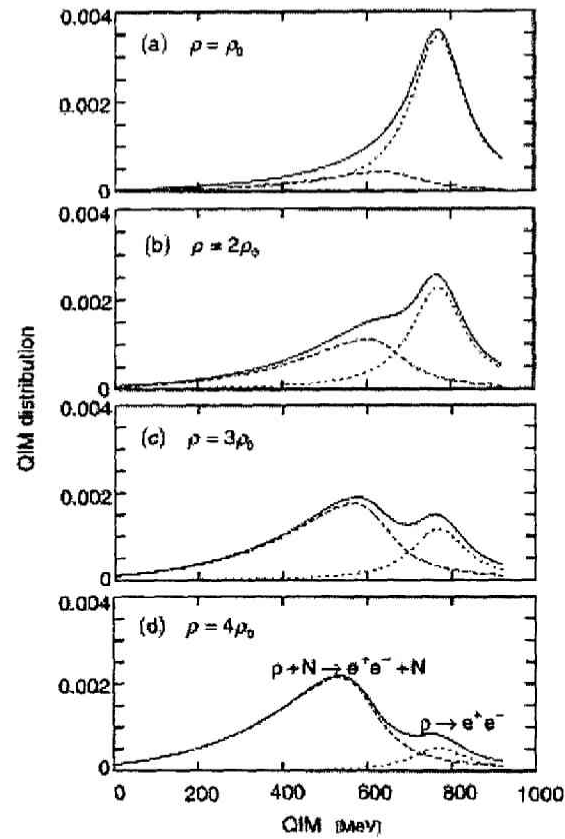This toy-model calculation is too simple in many aspects. For example,

Figure 4.6: Spectra function of ρ meson decay in the nuclear medium with various density [41]. No medium mass modification is assumed. The dotted curves are for normal decay ($\rho \to e^+e^-$), whereas the broken curves at lower mass represent pseudo peaks produced from two-body-correlation decay process.

we assumed the production point of the ρ/ω mesons is surface of a nucleus, which is not at all obvious, and to be more realistic we have to take the formation time of the mesons into account. If we consider the formation time, the decay point of the ρ/ω mesons is shifted and the excess for the carbon target would be suppressed.
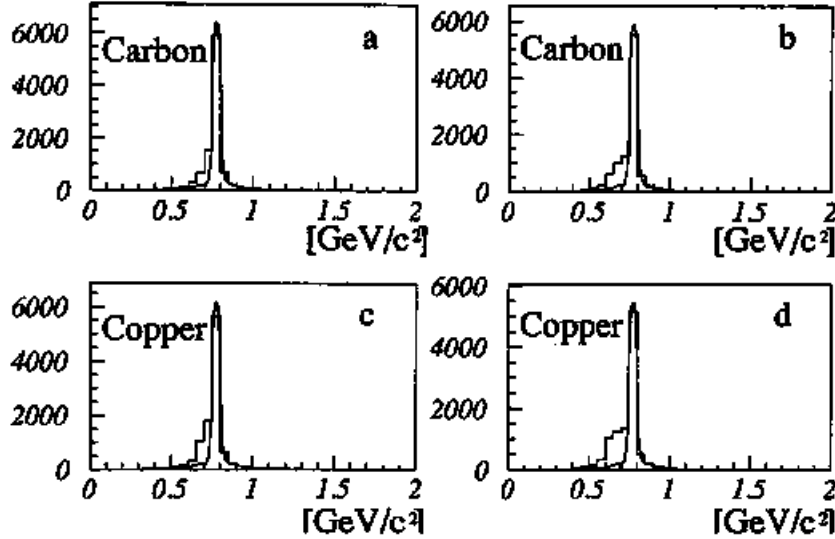
Figure 4.7: Expected invariant mass spectra of $\rho/\omega \to e^+e^-$: upper histogram for the carbon and lower histogram for the copper targets, left side histogram (a and c) corresponds to mass decrease of 120 MeV/c^2 and right side histogram corresponds to mass decrease of 180 MeV/c^2 (b and d). We assumed 3 times larger decay width of ρ/ω meson in nuclear medium.

Although the toy-model approach is remarkable, many things have to be investigated theoretically and experimentally to draw a conclusion on the origin of the observed excess. Theoretically, more realistic calculation on the collisional broadening must be investigated, the ρ/ω interference in nuclear media is not studied at all, and the calculation of the spectral function of the ρ/ω mesons in this kinematical region is waited. Experimentally, we need more statistics to determine the modified mass shape and the amount of the excess more accurately. Higher statistics will allow us to study the momentum dependence of the observed excess, which can provide the new type of data to be called as in-media dispersion relation of vector mesons.

Width	C or CH2 N_{excess}/N_{omega}	Copper N_{excess}/N_{omega}
X 1.0	0.20 ± 0.04	0.29 ± 0.04
X 3.0	0.34 ± 0.06	0.50 ± 0.10
X 7.0	0.57 ± 0.13	0.91 ± 0.20
X 10.0	0.71 ± 0.17	1.16 ± 0.28
X 15.0	0.94 ± 0.24	1.56 ± 0.44
experiment	0.26 ± 0.16	1.48 ± 0.56

Table 4.2: The result of the toy-model calculation. The errors correspond to the theoretical uncertainty given by Hatsuda and Lee.

Further analysis and data accumulation of the present experiment is underway, which will shed brighter light on this exciting field of physics.

Chapter 5

Conclusion

We have measured the e^+e^- invariant mass spectra in 12-GeV p+A interaction at KEK Proton Synchrotron. The goal of the experiment is to observe a signature of the partially-restored chiral-symmetry appearing as modification of the mass of vector mesons.

To increase a sensitivity to in-medium decays of the vector mesons, the present experiment was designed to cover the target rapidity region (0.6 $< y_{ee} < 2.2$) and to detect slowly moving vector mesons whose $\beta\gamma_{lab}$ was from 1 to 3. A significant portion of such vector mesons should decay inside a nucleus, and the deformation of the mass spectra was expected to be observed.

The spectrometer was newly constructed at the high-intensity primary beam-line to detect the $\phi \to e^+e^-$, $\rho/\omega \to e^+e^-$ and $\phi \to K^+K^-$ channels simultaneously. The results presented in this paper have been obtained from the data taken in May 1998. The analysis were performed in the e^+e^- channel. For the electron identification, the gas Čerenkov counter and the lead-glass EM calorimeters were used. For electrons with a momentum greater than 400 MeV/c, the overall efficiencies including the trigger threshold and the off-line cut were 55% for front gas-Čerenkov counters (FGC), 86% for rear gas-Čerenkov counters (RGC) and 85% for the calorimeters, rear lead-glass EM calorimeters (RLG) and side lead-glass EM calorimeters (SLG). We achieved the π meson rejection of 6.7×10^{-4} with a cascade operation of FGC and the EM calorimeters, and 3.9×10^{-4} with FGC and RGC for 400 MeV/c π mesons.

We have obtained 610 e^+e^- samples over three targets (polyethylene, carbon and copper). The remaining fake electron pair such as $e^-\pi^+$ or $e^+\pi^-$ was

estimated to be about 13% and the contaminations like $\pi^+\pi^-$ to be negligibly small. The invariant mass resolution of 1.8 MeV/c^2 and 3.6 MeV/c^2 was achieved in the measurement of the $\Lambda \rightarrow p + \pi^-$ and $K_s \rightarrow \pi^+ + \pi^-$ decays, respectively, and the mass resolution of the ω and ϕ meson was obtained to be 9.6 MeV/c^2 and 12.0 MeV/c^2, respectively.

We observed a clear peak of the ω meson and a peak of the ϕ meson decaying into e^+e^- for each target. We obtained 75.5 $\pm$ 9.0 ω and 7.4 $\pm$ 5.8 ϕ from the light target and 20.0 $\pm$ 4.8 ω and 5.2 $\pm$ 2.7 ϕ from the copper target. A significant shape difference is observed between the light nuclear targets and the copper target as an excess at the low mass side of the ω peak. We have tried to reproduce the mass shape of the obtained spectra with the combinatorial background and the known hadronic sources. The relative abundances of the known sources and the combinatorial background were obtained through the fit.

The excess in the mass region from 550 MeV/c^2 to 750 MeV/c^2 was evaluated. The number of excess of the light target is 19.6 $\pm$ 11.7 and that of the copper target is 29.5 $\pm$ 8.7. The excess is statistically significant for the copper target data. The ratios to the amplitude of the ωpeak are 0.26 $\pm$ 0.16 for the light target and 1.48 $\pm$ 0.56 for the copper target. The difference between the two cases should be originated from the difference of the nuclear size. The natural explanation of the shape change is that the mass modification of ρ/ω mesons takes place inside a nucleus. Although the mass shape of the modified meson is difficult to be predicted and the trivial effect like the collisional broadening was not perfectly ruled out, it should be noted that the excess in the copper target data is visible in the mass range about 200 MeV below the ω peak being consistent with the expected shift predicted by Hatsuda and Lee.

We have observed a signature of in-medium mass modification of ρ/ω meson. This is the first observation of the leptonic in-medium decay of the vector mesons at normal nuclear-matter density.

Acknowledgement

I would like to acknowledge so many people who are essential to complete the present work. I have been supported by a number of people during my years in the graduate school, Kyoto University.

First of all, I would like to express my sincere and special thanks to Professor Hideto En'yo who has been my supervisor. Without his introduction, I would not even have my teeth into nuclear physics experiment. He has continuously encouraged, advised, and supported me at every stage of the work: experiment, analysis and publication. I have been deeply influenced from his gratitude to study science and physics.

I am gratefully acknowledge Prof. A. Masaike. He has been encouraging me since my time in the undergraduate course. His continual and tireless support has ensured that my years spent in the undergraduate and the graduate courses has been worthwhile and fulfilling. Under his guidance, I have had opportunity to participate in a wide range of projects in many areas of experimental physics.

Special thanks are due to Prof. K. Imai for his guidance, fruitful discussions, and zealous support in many aspects. He has encouraged me to brush up the physical insights and complete the doctoral dissertation.

I am grateful to Prof. H. Hamagaki, the leader of the group in which I am now working, who have encouraged me to complete this doctoral work. He is collaborating with me and giving me many suggestions on study of physics.

I wish to acknowledge all the collaborators of the E325 experiment. My work would never be completed without their great efforts. I express my thanks to Prof. J. Chiba. He has provided clear and helpful advice at stages of the data-taking and analysis. I owe Prof. M. Ieiri and Prof. K.H. Tanaka, who constructed and maintained the EP1B beam line, for their help and useful advice. I appreciate Ms. M. Sekimoto, without her supports and advice I would never finish the construction of the drift chambers.

study.

Appendix A

Combinatorial background

The combinatorial background was originated from two tracks, which were picked up from two independent Dalitz decays of π or γ conversions, and the pairs like $e^-\pi^+$ or $e^+\pi^-$ due to the particle misidentification. If there is no correlation between two tracks of the combinatorial background, the distribution of the combinatorial background was obtained from the event mixing method.
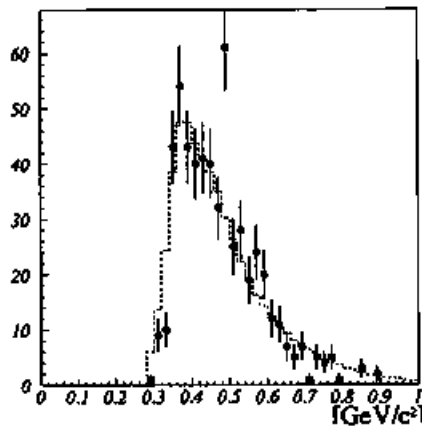

Figure A.1: Invariant mass spectrum of $\pi^+\pi^-$ The dotted line corresponds to the combinatorial background which obtained by the event mixing method.

There is a possibility of the existence of the correlation between two π's in the same event, because of the limited phase space of the present experiment. Thus, the correlation of the two π's in the same event had to be checked on

the invariant mass spectrum of $\pi^+\pi^-$ pairs. Figure A.1 shows the invariant mass spectrum of $\pi^+\pi^-$ pairs. As described in the section 3.3.3, the clear peak of K_s decaying $\pi^+\pi^-$ is visible in the spectra. The background was well reproduced by the combinatorial background which was obtained from the event mixing method. This means two π's in the same event is uncorrelated.

The details of the event mixing method is described below. The tracks which used in the event mixing were taken from the final sample events. For the correction of the influence of the correlated track, which were from ω peak, the tracks, which were reconstructed to the ω peak region, were reduced in the event mixing. The mixing of the tracks was done with the same target events. Thus, the distribution of the combinatorial background was made for the each target. The statistics of the each distribution were about 10000.

The abundance of the combinatorial background was checked through the fit. We fit the histograms above 1 GeV/c^2 with the combinatorial background only. The result of the fit was consistent of 10% with the result of the fit on all region.

Bibliography

[1] B.B. Back *et al.* (PHOBOS Collaboration), Phys. Rev. Lett. **85** (2000) 3100-3104.
See also http://www.rhic.bnl.gov/

[2] http://cern.web.cern.ch/CERN/Announcements/2000/NewStateMatter/

[3] H. Berker *et al.*, Phys. Rev. Lett. **74** (1995) 3340-3343.
I.G. Bearden *et al.*, Phys. Rev. Lett. **78** (1997) 2080-2083.
I.G. Bearden *et al.*, Phys. Lett. **B471** (1999) 6-12.

[4] G. Agakichiev *et al.*, Phys. Lett. **B422** (1998) 405-412.
B. Lenkeit *et al.*, Nucl. Phys. **A654** (1999) 627c-630c.
B. Lenkeit *et al.*, Nucl. Phys. **A661** (1999) 23c-32c.

[5] T. Alber *et al.*, Phys. Rev. Lett. **75** (1995) 3814-3817.
H. Appelshäuser *et al.*, Eur. Phys. J. **C2** (1998) 661-670.
F Sikler *et al.*, Nucl. Phys. **A661** (1999) 45c-54c.

[6] M.C. Abreu *et al.*, Phys. Lett. **B410** (1997) 337-343.
M.C. Abreu *et al.*, Phys. Lett. **B450** (1999) 456-466.
M.C. Abreu *et al.*, Phys. Lett. **B477** (2000) 28-36.

[7] R. Klingenberg *et al.*, Nucl. Phys. **A610** (1996) 306c-316c.
G. Ambrosini *et al.*, Phys. Lett. **B417** (1998) 202-210.
G. Ambrosini *et al.*, New Journal of Physics **1** (1999) 22.1-22.23.

[8] E. Anderson *et al.*, Phys. Lett. **B449** (1999) 401-406.
F Antinori *et al.*, Nucl. Phys. **A661** (1999) 130c-139c. F. Antinori *et al.*, Eur. Phys. J. **C14** (2000) 633-641.

[9] R. Albrecht *et al.*, Phys. Rev. Lett. **76** (1996) 3506-3509.
M.M. Aggarwal *et al.*, Phys. Rev. Lett. **81** (1998) 4087-4091; **84** (2000) 578-579(E)
M.M. Aggarwal *et al.*, Phys. Rev. Lett. **83** (1999) 926-930.

[10] G.Q. Li *et al.*, Phys. Rev. Lett. **75** (1995) 4007.

[11] C.M. Ko *et al.*, Nucl. Phys. **A610** (1996) 342c.

[12] G.E. Brown and M. Rho, Phys. Rev. Lett. **66** (1991) 2720.

[13] T. Hatsuda and S.H. Lee, Phys. Rev. **C46** (1992) R24.

[14] M. Asakawa and C.M. Ko, Phys. Rev. **C48** (1993) R526.

[15] E.G. Drukarev and E.M. Levin, Prog. Part. Nucl. Phys. **27** (1991) 77.

[16] G.J. Lolos *et al.* (TAGX Collaboration), Phys. Rev. Lett. **80**:241-244 (1998).

[17] R.J. Porte *et al.*, Phys. Rev. Lett. **79** (1997) 1229.

[18] W. Schoen *et al.* (HADES Collaboration), Acta Phys. Polon. **B27**:2959-2963 (1996).

[19] GSI/SIS proposal S214, Search for bound η- and ω- nuclear states using the recoilless $(d, ^3 He)$ reaction.

[20] T. Nakano *et al.*, Nucl. Phys. **A629**, 559c (1998).

[21] KEK-PS E325 proposal
(http://www.pn.scphys.kyoto-u.ac.jp/phi/E325_project.html).

[22] D. Cabera *et al.*, nucl-th/0011037

[23] M. Binkley *et al.*, Phys. Rev. Lett. **37**, 571 (1976).
T. Tabaru (E325) thesis for Kyoto Univ., in preparation.

[24] M. Takasaki *et al.*, KEK Internal 95-1.

[25] I.Adachi *et al.*, Nucl. Instr. and Meth. **A335** (1995) 390.

[26] M. Ishino *et al.*, Nucl. Instr. and Meth. **A457** (2001) 581.

[27] Y. Sugaya *et al.*, Nucl. Inst. and Meth. **A368** (1996) 635.

[28] Vector Fields Limited (UK), http://www.vectorfields.co.uk/

[29] developed in CERN. http://consult.cern.ch/writeup/garfield/

[30] M. M. Morii *et al.*, KEK Preprint 88-80 November 1988.

[31] H. Hinterberger and R. Winston, Rev. Sci. Instr. **37**, 1004 (1966)

[32] VMEbus architecture, IEEE 1014/D1.0.

[33] T. K. Ohsuka *et al.*, KEK report 85-10 (1985)

[34] Unidaq Documentation Set, SDC-93-487, Superconducting Super Collider Laboratory, 1993.

[35] developed in CERN. http://consult.cern.ch/writeup/minuit/

[36] Y. Nara *et al.*, Phys. Rev. **C61**:024901 (1999).

[37] A. Faessler, C. Fuchs and M. I. Krivoruchenko, Phys. Rev. C61:035206,2000

[38] V Blobel *et al.*, Phys. Lett. **B48**, 73 (1974).

[39] F Klingl *et al.*, Nucl. Phys. **A624** (1997) 527-563.

[40] E.L. Bratkovskaya *et al.*, Nucl. Phys. **A653** (1999) 301-317.

[41] T. Yamazaki and Y. Akaishi, Phys. Lett. **B453** (1999) 1-6.